Check for updates

International Journal of Micro Air Vehicles

Review

International Journal of Micro Air Vehicles
Volume 12: 1–22
© The Author(s) 2020
Article reuse guidelines:
sagepub.com/journals-permissions
DOI: 10.1177/1756829320914264
journals.sagepub.com/home/mav
SAGE

Model-free control algorithms for micro air vehicles with transitioning flight capabilities

Jacson MO Barth[1], Jean-Philippe Condomines[1], Murat Bronz[1], Jean-Marc Moschetta[2], Cédric Join[3,4] and Michel Fliess[4,5]

Abstract

Micro air vehicles with transitioning flight capabilities, or simply hybrid micro air vehicles, combine the beneficial features of fixed-wing configurations, in terms of endurance, with vertical take-off and landing capabilities of rotorcrafts to perform five different flight phases during typical missions, such as vertical takeoff, transitioning flight, forward flight, hovering and vertical landing. This promising micro air vehicle class has a wider flight envelope than conventional micro air vehicles, which implies new challenges for both control community and aerodynamic designers. One of the major challenges of hybrid micro air vehicles is the fast variation of aerodynamic forces and moments during the transition flight phase which is difficult to model accurately. To overcome this problem, we propose a flight control architecture that estimates and counteracts in real-time these fast dynamics with an intelligent feedback controller. The proposed flight controller is designed to stabilize the hybrid micro air vehicle attitude as well as its velocity and position during all flight phases. By using model-free control algorithms, the proposed flight control architecture bypasses the need for a precise hybrid micro air vehicle model that is costly and time consuming to obtain. A comprehensive set of flight simulations covering the entire flight envelope of tailsitter micro air vehicles is presented. Finally, real-world flight tests were conducted to compare the model-free control performance to that of the Incremental Nonlinear Dynamic Inversion controller, which has been applied to a variety of aircraft providing effective flight performances.

Keywords

MAV with transitioning flight capabilities, hybrid MAVs, control system architecture, flight control, model-free control

Date received: 26 April 2019; Revised 6 December 2019; accepted: 13 February 2020

Introduction

Micro air vehicles (MAVs) with transitioning flight capabilities, or simply hybrid MAVs, operate over a wide flight envelope including different flight phases, such as vertical take-off, efficient forward flight, transitioning flights, hovering and vertical landing, see Figure 1. While this complete flight envelope enlarges the application range of MAVs, new aerodynamics optimization approaches must be developed to improve the MAV flight performance, considering the aerodynamics challenges of each flight domain. Furthermore, the autopilot system must ensure the stability and the tracking of trajectories for all these flight domains which results in a higher degree of challenge and complexity also for the guidance, navigation, and control community. Different hybrid MAV configurations such as tilt-rotors[1] or tilt-wings,[2] quadplanes,[3] and tilt-body or tailsitter[4] can be found in literature.

[1]ENAC, Université de Toulouse, Toulouse, France
[2]Department of Aerodynamics, Energetics and Propulsion, ISAE-Supaero, Toulouse, France
[3]CRAN, Université de Lorraine, Vandœuvre-lès-Nancy, France
[4]AL.I.E.N (ALgèbre pour Identification & Estimation Numérique), Vézelise, France
[5]LIX, École Polytechnique, Palaiseau, France

Corresponding author:
Jacson MO Barth, UAV Systems Group, ENAC, Université de Toulouse, France.
Email: jacson-miguel.olszanecki-barth@enac.fr

Creative Commons Non Commercial CC BY-NC: This article is distributed under the terms of the Creative Commons Attribution-NonCommercial 4.0 License (https://creativecommons.org/licenses/by-nc/4.0/) which permits non-commercial use, reproduction and distribution of the work without further permission provided the original work is attributed as specified on the SAGE and Open Access pages (https://us.sagepub.com/en-us/nam/open-access-at-sage).

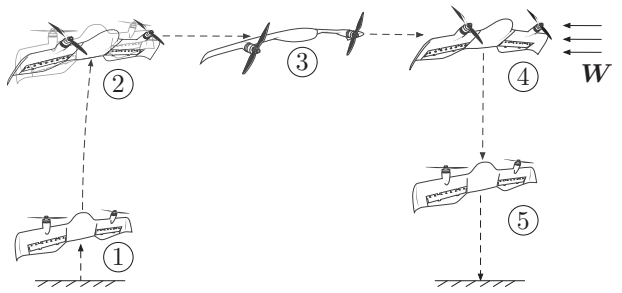


Figure 1. Typical flight phases of micro air vehicles with transitioning flight capabilities: 1 – Vertical take-off; 2 – Transition; 3 – Forward flight; 4 – Hover flight; 5 – Vertical landing. The vector ***W*** represents the wind disturbances.

These platforms have been designed in order to solve the aerodynamics and mechanical limitations of each of them, and the choice of the appropriated MAV configuration varies according to the imposed flight mission specifications, e.g., maximum payload, the desired endurance and range, etc. Generally, hybrid MAVs are designed and optimized to perform an efficient forward flight, since this flight phase represents most of its mission. Various studies have improved and assessed the aerodynamic properties of hybrid MAVs previously.[5,6] A critical point is the design of flap effectiveness which needs to be optimized in order to create sufficient pitch moment ensuring the control authority during transitioning flights. We focus this research project in the design and control of tailsitter MAVs, and we investigate the performance of this peculiar MAV class for three reasons: (1) Tailsitters have a better endurance in forward flight when compared to other configurations of hybrid MAVs; (2) The simple transition mechanism of tailsitters facilitates the control design for its entire flight envelope, unlike to tiltrotors that need additional actuators to orient the propeller in order to perform transitioning flights; (3) The design of controllers requiring little prior knowledge of the dynamics of tailsitter MAVs remains an attractive, motivating and challenging topic that needs to be answered by the control community. Typically, the entire flight envelope of tailsitter MAVs can be analyzed in three distinct flight modes, namely, hovering flight, forward flight and transitioning flight. The stabilization of hovering and forward flights can be achieved using linearized models around an equilibrium point facilitating the implementation of classical linear control algorithms. On the other hand, transitioning flights present some peculiarities that include fast changing of aerodynamic forces and moments with wing behaviors partially stalled. Based on such aerodynamic effects, the identification of a reliable model that accurately represents the nonlinear dynamics of a tailsitter MAV over its entire flight envelope remains an expensive, a time consuming and a difficult task. Because of these practical problems related to the characterization of a model for the design of model-based controllers, some research works considered the transition flight as an undesirable and transient flight phase. However, transitioning flights need to be continuously stabilized in order to ensure a smooth and safe flight, especially for flying missions in windy environments. Hybrid MAVs are often considered by the control community as a parameter varying system, e.g. the change of aerodynamic coefficients according to the hybrid MAV attitude orientation and the environmental wind conditions. Consequently, designing a control technique for autopilot systems that does not rely on prior knowledge of the hybrid MAV model becomes an intuitive, innovative and, from the point of view of the authors, an appropriate control methodology. Therefore, the development of such a controller that estimates the hybrid MAV dynamics and counteracts it, in real time, can be easily adaptable and implemented for different hybrid MAVs.

Literature review

Different control strategies have been designed for hybrid MAVs; we present some of them in the following with particular emphasis in the controllers developed for the tailsitter class. For practical reasons, classical linear controllers designed using PID techniques have been applied in the control of hybrid MAVs.[7–11] Although simple to tune without the knowledge of the controlled system, PID controllers have insufficient robustness properties against wind disturbances. Autopilot systems designed from optimal control theory, have been researched.[12,13] For instance, the linear quadratic regulator which was designed and applied for a tailsitter MAV previously modeled and identified from wind tunnel campaign.[14] However, the performance of model-based controllers may differ primarily in the fidelity with which the plant is modeled and the accuracy of the identified model parameters. Hence, classical model-based control techniques seem to be neither optimal for hybrid MAVs nor easily transposable for a new platform. Gain scheduling methods employing different control algorithms with both linear[15] and nonlinear approaches,[16] have been developed to stabilize hybrid MAVs at different pitch angle orientations within the transitioning flight. Gain scheduling techniques allow easy understanding and simple implementation of the control gains that cover the entire flight envelope of hybrid MAVs. However, the principal disadvantage of this control method, found in literature,[17] is the expensive computational

cost for operations in real time. In the same way, an attitude controller based on optimal control algorithms was proposed by Ritz and Andrea,[18] different control solutions for a set of attitude errors were precomputed and stored in a lookup table. According to the current flight conditions and for each autopilot system update, the desired control gains are obtained by reading their predefined values in the table. Further analysis is needed to determine if this proposed control strategy can be effective and easily adaptable for different hybrid MAVs. Adaptive control techniques which account for uncertainties present in the hybrid MAV model were developed by some authors.[19,20] However, instability problems with adaptive control methods can still exist with regard to unmodeled dynamics or inaccurate models used in the adaptation criterion of controller's gains. Different research topics applying nonlinear control techniques on hybrid MAVs, such as backstepping,[19,21,22] NDI[20,23,24] and INDI,[25] appears to be positively researched in literature. The INDI approach, which is a control that depends less on the model, was experimentally flight tested providing excellent performance against wind disturbances. This controller requires the identification of the system actuator behavior in order to estimate its control effectiveness. As the actuator's effectiveness varies according to the flight phase, e.g. hovering or forward flight, a gain scheduling method was implemented to fit the actuator effectiveness under the respective flight domain. Some theoretical research has analyzed the performance of nonlinear feedback control on axisymmetric aerial vehicles[26] proposing an extended control solution to a larger set of generic aerodynamic models[27] which could include hybrid MAVs. Additionally, a variety of nonlinear control strategies based on Lyapunov's stability concepts have been designed to hybrid MAVs.[4,28]

Links with the model-free control algorithm

The literature presents some particular control algorithms that do not rely on modeling. For instance, the model-free control (MFC) approach proposed by Fliess and Join[29] has been successfully illustrated in different concrete case-studies varying from wastewater denitrification,[30] nanopositioning of piezoelectric systems[31] up to inflammation resolution in biomedical applications,[32] see also its references for additional case-study examples and supplementary information. Some research works based on MFC techniques have led to patents, such as Join et al.[33] and Abouaïssa et al.[34] This control approach has been applied in the aerospace field[35,36] and, except for our previous work, it has never been applied on hybrid MAVs which is an additional motivation for the development of our research project. The advantage of the control methodology proposed in this paper is the capability to estimate the hybrid MAV dynamics, without a prior knowledge of its parameters, only from its output and input-control signal measurements. Thus, the disturbances that may affect flight performances are measured and the MFC algorithms are able to estimate as well as counteract the undesirable dynamics in order to continuously stabilize the hybrid MAV for arbitrary attitude orientations covering its entire flight envelope.

Present work

The main contribution of our current work is to develop a fully autonomous MAV with transitioning flight capabilities that performs a given mission accurately. Depending upon the mission complexity and its requirements, the MAV should fly at low and high air speeds, respectively corresponding to hovering and forward flight phase. Based on these mission requirements, and the modeling issue presented in the previous section involving this particular MAV class, we present a part of our previous work that deals with:

(i) comparison between a model-based controller and our MFC architecture during the transition flight in a disturbed environment;[37]
(ii) uncertain parameter analysis of fixed-wing MAVs in forward flight;[38]
(iii) full MFC architecture for position tracking, velocity control and attitude stabilization of a hybrid MAV during its entire flight envelope;[39]

Our intention is to analyze our control architecture through additional flight simulations and real-world flight tests in order to investigate its operational behavior, its limits and the interaction between each MFC control block. The new contributions of this paper, with respect to our previous works, are:

(i) initial condition analysis during hovering and transitioning flight phases in order to empirically determine a safe and stable boundary for distinguished initial conditions of attitudes and velocities;
(ii) control performance analysis in the frequency domain during hovering and forward flights;
(iii) study of MFC's adaptive properties for parametric variation illustrations during the forward-to-hover transition through flight simulations;
(iv) real-world flight tests to compare the MFC attitude stabilization performance to that of the INDI controller in indoor flight conditions;

The paper is organised as follows: in the next section, we present the manufacturing process and the particular aerodynamics of the hybrid MAV prototype named DarkO. Then, we describe the hybrid MAV behavior from a mathematical formulation based on equations of motion. This is followed by a section in which the control strategy is detailed as well as the proposed control architecture. Flight simulations are presented then and real-world flight tests follow. Finally, the reader can find the conclusion and the future work.

Hybrid MAV prototype

Throughout the whole study, we have used the DarkO vehicle which is a tailsitter configuration consisting of two motors, positioned in front of the wing, and two exceptionally large double-flapped control surfaces. Mission definition of DarkO has been mainly optimized for forward flight with the capability of taking off and landing vertically. Therefore, it has not been particularly designed for hovering for long duration.

Manufacturing

The DarkO's frame is completely manufactured by the 3D printing method using Onyx material. Figure 2 shows the printed pieces that are assembled in order to build the whole frame. The shell structure for the wing and the fuselage halves are manufactured as 0.7 mm thick skins, and the spar is manufactured with the addition of unidirectional concentric carbon fibers embedded into Onyx material. This method ensures to have a sufficiently rigid airframe that supports aerodynamic forces and yet also flexible enough to absorb harsh impacts during landing and test flights.

Control surface design

A particular feature that is required by the tailsitter configuration is to generate excessive amount of pitching moment in order to transition mainly from forward flight phase to hovering flight phase. Therefore, DarkO frame's control surfaces have been designed as double-flap which has a passive mechanical constant ratio. Traditionally, multi-section flaps have been designed for lift enhancement; however, in our case the design objective is to generate as much positive pitching moment as possible without having a massive flow separation on the bottom surface of the airfoil. The advantage of using double-flap (δ_{II}) control surface with respect to using a single-flap (δ_I) control surface has been shown in Figure 3. Variation of the sectional lift C_l, drag C_d, and moment coefficients C_m at different flap deflection angles have been compared for the two different flap configurations. The analysis has been done by using the open-source program XFOIL.[40] Reynolds number used during the analysis corresponds to the slipstream velocity seen by the blown portion of wing and is approximately 150k. The DarkO's motor mounts have an incidence angle of –6 degrees on DarkO's wings; therefore, the airfoil has been set to an angle of attack of + 6 degrees and then the flap angle has been varied between –2 and –14 degrees (negative flap angle being upward). Particular attention should be given to the pitching moment C_m in the figure. We notice that double-flap (δ_{II}) control surface

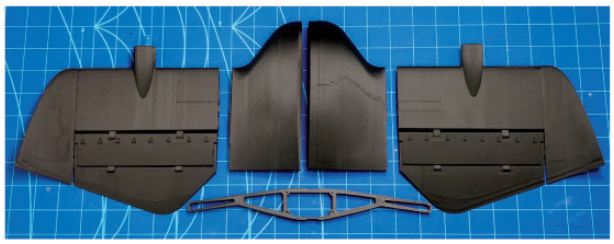


Figure 2. Printed parts of DarkO out of Onyx material.

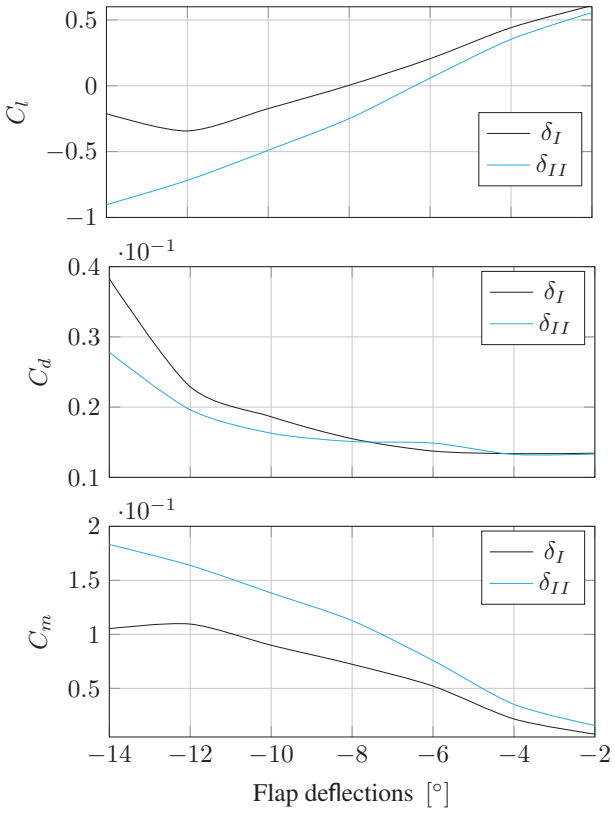


Figure 3. Variation of the sectional lift C_l, drag C_d, and moment coefficients C_m with respect to flap angles for different flap configurations: double-flap (δ_{II}) control surface and a single-flap (δ_I) control surface

can generate almost two times the pitching moment generated by the single-flap (δ_I) control surface. As a side effect, the double-flap control surface also works efficiently for lift generation; however, as we are trying to increase the pitching moment (in positive direction), the lift generation happens in negative direction. The vehicle requires the excessive amount of pitching moment only during transition phase, and the duration of this maneuver is very short; therefore, lift reduction caused while increasing the pitching moment has not been taken as an issue.

Simplified tailsitter MAV model

This section is divided into two parts. First, we present the mathematical formulation of aerodynamic forces and moments, and the aerodynamic assumptions used in the hybrid MAV model. Then, the equations of motion, based on Newton's second law, are introduced to describe the hybrid MAV behavior. The obtained hybrid MAV dynamics are used to establish a flight simulator in order to analyze the proposed control approach before real-world flight tests.

Formulation of aerodynamic forces and moments

We present an analytic continuous singularity-free formulation of aerodynamic forces $\boldsymbol{F}_{a_b} \in \mathbb{R}^3$ and moments $\boldsymbol{M}_{a_b} \in \mathbb{R}^3$ acting in a wing over a complete 360° angle of attack, based on previous work proposed by Lustosa et al.[41] The wing with a surface S, is immersed in an incompressible and inviscid airflow with air density ρ. The free-stream velocity is composed by the linear element $\boldsymbol{v}_\infty \in \mathbb{R}^3$ and the angular component defined by $\boldsymbol{\omega}_\infty \in \mathbb{R}^3$ which, in the absence of wind, is equal to the hybrid MAV angular velocity $\boldsymbol{\omega_b} \in \mathbb{R}^3$. This formulation of aerodynamic forces and moments is given by

$$\begin{pmatrix} \boldsymbol{F}_{a_b} \\ \boldsymbol{M}_{a_b} \end{pmatrix} = -\frac{1}{2}\rho S \eta C \Phi(\boldsymbol{\eta_b}) C \boldsymbol{\eta_b} \tag{1}$$

where

$$\eta = \sqrt{v_\infty^2 + \mu c^2 \omega_\infty^2}, \quad \text{with} \quad \mu \in \mathbb{R} > 0 \tag{2}$$

and

$$\boldsymbol{\eta_b} = \begin{pmatrix} \boldsymbol{v}_\infty \\ \boldsymbol{\omega}_\infty \end{pmatrix} \tag{3}$$

The vector $\boldsymbol{\eta_b}$ describes the linear and angular free-stream velocities in the body coordinate frame. The matrix C denotes the reference wing parameters in an extended representation

$$C = \begin{pmatrix} I_{3\times3} & 0_{3\times3} \\ 0_{3\times3} & \begin{bmatrix} b & 0 & 0 \\ 0 & c & 0 \\ 0 & 0 & b \end{bmatrix} \end{pmatrix} \tag{4}$$

where b and c are, respectively, the wingspan and the mean chord. Finally, the matrix $\Phi \in \mathbb{R}^{6\times6}$, which is subdivided into four matrices $\Phi^{(\cdot)} \in \mathbb{R}^{3\times3}$, shows the interaction between aerodynamic forces and moments with linear and angular free-stream velocities

$$\Phi = \begin{pmatrix} \Phi^{(fv)} & \Phi^{(fw)} \\ \Phi^{(mv)} & \Phi^{(mw)} \end{pmatrix} \tag{5}$$

The Φ parameters are deduced from thin airfoil theory; we refer the interested reader to Lustosa[42] for further information. Nonetheless, we mention that

$$\Phi_0^{(fv)} = \begin{pmatrix} C_{d0} & 0 & 0 \\ 0 & C_{y0} & 0 \\ 0 & 0 & 2\pi + C_{d0} \end{pmatrix} \tag{6}$$

$$\Phi^{(f\omega)} = \begin{pmatrix} 0 & 0 & 0 \\ 0 & 0 & b^{-1}\Delta r C_{y0} \\ 0 & -c^{-1}\Delta r(2\pi + C_{d0}) & 0 \end{pmatrix} \tag{7}$$

$$\Phi_0^{(mv)} = \begin{pmatrix} 0 & 0 & 0 \\ 0 & 0 & -c^{-1}\Delta r(2\pi + C_{d0}) \\ 0 & b^{-1}\Delta r C_{y0} & 0 \end{pmatrix} \tag{8}$$

$$\Phi^{(m\omega)} = \frac{1}{2}\begin{pmatrix} C_{l_p} & C_{l_q} & C_{l_r} \\ C_{m_p} & C_{m_q} & C_{m_r} \\ C_{n_p} & C_{n_q} & C_{n_r} \end{pmatrix} \tag{9}$$

with C_{d0} the minimal drag coefficient and C_{y0} the minimal side force coefficient. The parameter Δr represents the distance between the center of gravity location and the aerodynamic center (neutral point). The negative values of Δr, according to the defined coordinate system, imply a positive static margin of the hybrid MAV. Finally, C_l, C_m and C_n are the aerodynamic moment coefficients which depend on the angular hybrid MAV velocities (p, q, r). The lift curve slope corresponding to 2π, in equations (6), (7) and (8), was deduced from the thin airfoil theory in 2D.

In this work, we evaluate the lift curve slope in 3D considering the wing aspect ratio (AR). According to Diederich's formula, we consider

$$\Phi_0^{(fv)}(:,3) = \begin{pmatrix} 0 \\ 0 \\ \dfrac{\pi AR}{1+\sqrt{1+(\frac{AR}{2})^2}} + C_{d0} \end{pmatrix} \tag{10}$$

$$\Phi^{(f\omega)}(:,2) = \begin{pmatrix} 0 \\ 0 \\ -c^{-1}\Delta r(\dfrac{\pi AR}{1+\sqrt{1+(\frac{AR}{2})^2}} + C_{d0}) \end{pmatrix} \tag{11}$$

$$\Phi_0^{(mv)}(:,3) = \begin{pmatrix} 0 \\ -c^{-1}\Delta r(\dfrac{\pi AR}{1+\sqrt{1+(\frac{AR}{2})^2}} + C_{d0}) \\ 0 \end{pmatrix} \tag{12}$$

where

$$AR = \frac{b^2}{S} \tag{13}$$

Finally, the flap deflections are modeled as varying cambered airfoils and the aerodynamic forces and moments created by these deflections are approximated by the following equations

$$\Phi^{(fv)}(\delta_i) = \Phi_0^{(fv)}(I - [\boldsymbol{\xi_f}]_\times \delta_i) \tag{14}$$

$$\Phi^{(mv)}(\delta_i) = \Phi_0^{(mv)}(I - [\boldsymbol{\xi_m}]_\times \delta_i) \tag{15}$$

the flap deflection effectiveness is represented by two skew-symmetric matrices, $[\boldsymbol{\xi_f}]_\times$ for the force effectiveness and $[\boldsymbol{\xi_m}]_\times$ for the moment effectiveness, given by

$$[\boldsymbol{\xi_f}]_\times = \begin{bmatrix} 0 & -\xi_f & \xi_f \\ \xi_f & 0 & -\xi_f \\ -\xi_f & \xi_f & 0 \end{bmatrix}$$

$$[\boldsymbol{\xi_m}]_\times = \begin{bmatrix} 0 & -\xi_m & \xi_m \\ \xi_m & 0 & -\xi_m \\ -\xi_m & \xi_m & 0 \end{bmatrix}$$

Equations of motion

The hybrid MAV model is divided into four rigid bodies (two propellers and two wings composing the fuselage) with constant mass (m), represented by 10 states $\boldsymbol{x} = (\boldsymbol{v_b}, \boldsymbol{\omega_b}, \boldsymbol{q})$, where $\boldsymbol{v_b} \in \mathbb{R}^3$ is the vehicle's linear velocity, $\boldsymbol{\omega_b} \in \mathbb{R}^3$ is the vehicle's angular velocity equals to $[p\,q\,r]^T$ both expressed in the body coordinate frame and $\boldsymbol{q} \in \mathbb{R}^4$ is the quaternion formulation. The system is controlled via four control-inputs, $\boldsymbol{u} = (\omega_l, \omega_r, \delta_l, \delta_r)$, respectively, the left and right propeller rotation speeds and the left and right flap deflections, which are represented in Figure 4.

In order to compute the forces and moments caused by the wing–propeller interaction, we define two segments. Each segment is composed of one wing j and one propeller k. Thus, the sum of aerodynamic forces acting on the wing j with the thrust $\boldsymbol{T}_k$ generated by the propeller rotation ω_k and the total moment described in the body coordinate frame, are given by

$$\boldsymbol{F_b} = \sum_{j,k=1}^{2} (\boldsymbol{F}_{\boldsymbol{a_{b_j}}} + \boldsymbol{T}_k) \tag{16}$$

$$\boldsymbol{M_b} = \sum_{j,k=1}^{2} (\boldsymbol{M}_{\boldsymbol{a_{b_j}}} + \boldsymbol{\tau_{b_k}} + \boldsymbol{p_p} \times \boldsymbol{T}_k + \boldsymbol{p_a} \times \boldsymbol{F}_{\boldsymbol{a_{b_j}}}) \tag{17}$$

The vector $\boldsymbol{p_p} = [p_{p_x}\, p_{p_y}\, p_{p_z}]^T$ defines the distance between the propeller k with the hybrid MAV center of mass. Both propellers are positioned symmetrically with respect to the hybrid MAV center of mass. The distance between the aerodynamic center and the center of mass is represented by the vector $\boldsymbol{p_a} = [p_{a_x}\, p_{a_y}\, p_{a_z}]^T$. The internal torque of the propeller $\boldsymbol{\tau_{b_k}}$ that is a

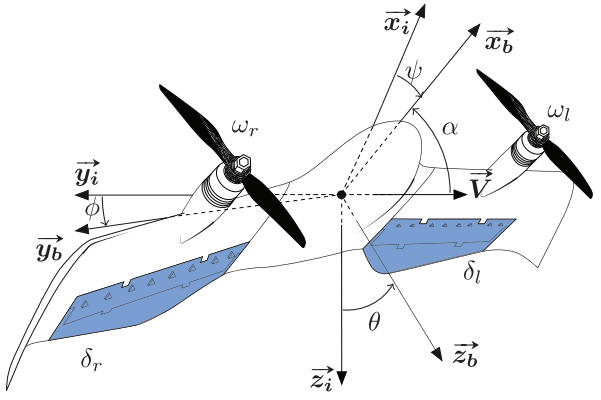


Figure 4. Illustration of the used coordinate frames, angles and actuators. The inertial coordinate frame is represented by $\mathcal{R}_i = \{\vec{x_i}, \vec{y_i}, \vec{z_i}\}$ and the body coordinate frame by $\mathcal{R}_b = \{\vec{x_b}, \vec{y_b}, \vec{z_b}\}$.

function of the vehicle's angular velocity $(p\,q\,r)$, and the thrust force $\boldsymbol{T}_k$, are defined by

$$\boldsymbol{T}_k = k_f \omega_k^2 \vec{\boldsymbol{x}_b}, \quad k_f \in \mathbb{R} > 0 \tag{18}$$

$$\boldsymbol{\tau}_{\boldsymbol{b}_k} = \boldsymbol{N}_{\boldsymbol{b}_k} - J_p(p + \omega_j)\begin{pmatrix} 0 \\ r \\ -q \end{pmatrix} \tag{19}$$

where

$$\boldsymbol{N}_{\boldsymbol{b}_k} = -\text{sign}(\omega_k) k_m \omega_k^2 \vec{\boldsymbol{x}_b}, \quad k_m \in \mathbb{R} > 0 \tag{20}$$

with k_f and k_m the propeller force and moment coefficients and $\boldsymbol{N}_{\boldsymbol{b}_k}$ the propeller moment. Equation (19) describes the gyroscopic interaction between the propellers and the fuselage with J_p equals to the propeller inertia. The vehicle's equations of motion are given by equation (21).

$$\begin{cases} m\dot{\boldsymbol{v}} & = R^T \boldsymbol{F}_{\boldsymbol{b}}(\boldsymbol{x}, \boldsymbol{u}, \boldsymbol{W}) + m\boldsymbol{g} \\ J\dot{\boldsymbol{\omega}}_{\boldsymbol{b}} & = \boldsymbol{M}_{\boldsymbol{b}}(\boldsymbol{x}, \boldsymbol{u}, \boldsymbol{W}) - [\boldsymbol{\omega}_{\boldsymbol{b}}]_\times J\boldsymbol{\omega}_{\boldsymbol{b}} \\ \dot{\boldsymbol{q}} & = \frac{1}{2}\boldsymbol{q} \otimes \boldsymbol{\omega}_{\boldsymbol{b}} \\ \dot{\boldsymbol{p}} & = \boldsymbol{v} \end{cases} \tag{21}$$

The gravitational acceleration vector is equals to $\boldsymbol{g} = g\vec{\boldsymbol{z}_i}$ and $\boldsymbol{W} \in \mathbb{R}^3$ is the wind disturbance vector. The rotation matrix R, namely the Direction Cosines Matrix (DCM, Note: The DCM can be defined with quaternion formulation.), represents the MAV rotation in three dimensions as a mathematical formulation. We assume that the hybrid MAV inertia matrix J is diagonal and it equals to $J = \text{diag}[J_{xx}\,J_{yy}\,J_{zz}]$. The position vector in the inertial coordinate frame is represented by $\boldsymbol{p} = [x\ y\ z]^T$. The highly maneuverable nature of the vehicle calls for a global numerically stable formulation of attitude and justifies the use of quaternions. The symbol $\otimes$ in the previous equation corresponds to the quaternion product. Supplementary Appendix A presents the tailsitter MAV parameters used in this work.

Control strategy

The proposed control strategy is based on MFC algorithms with no information about the tailsitter MAV parameters (e.g. mass, inertia, aerodynamics coefficients, etc.). This controller can be implemented on multiple-input multiple-output systems by assuming an approximate decoupling between the dynamics of the controlled system. This major assumption has been verified by different practical experiments.[43] Therefore, for simplicity reasons, we present the MFC algorithms for single-input single-output systems. We use a prior knowledge of sign-convention between control-input influence in the MAV states based on simple flight mechanics equations to develop the correct block interactions in the proposed control architecture. In terms of tuning model-based control approaches, the model given in the previous section is only used to simulate the tailsitter MAV dynamics and not for control design.

MFC principles

As introduced by Fliess and Join,[29] an unknown finite-dimensional system with a single control-input (u) and a single output (y) can be described by the following input/output relation in a differential equation formulation

$$\mathbb{E}\left(y, \dot{y}, \ldots, y^{(a)}, u, \dot{u}, \ldots, u^{(b)}\right) = 0 \tag{22}$$

where $\mathbb{E}$ is a polynomial function with real unknown coefficients. We can also describe

$$y^v = \mathbb{E}(t, y, \dot{y}, \ldots, y^{(v-1)}, y^{(v+1)}, \ldots, y^{(a)}, u, \dot{u}, \ldots, u^{(b)}) \tag{23}$$

with $0 < v \leq a$ and $\frac{\delta \mathbb{E}}{\delta y^v} \neq 0$. These unknown dynamics can be modeled by a purely numerical equation, so-called *Ultra-Local Model*

$$y_m^{(v)} = F_y + \lambda \cdot u \tag{24}$$

In equation (24), v is the order of the derivative of y_m, $\lambda \in \mathbb{R}$ is a non-physical constant parameter. Moreover, the exploitation of this numerical model requires the knowledge of F_y. This quantity represents the real dynamics of the model as well as the different disturbances which could damage the performance of the output-system. Thus, an accurate estimation of F_y, defined as $\hat{F}_y$, is crucial and plays an important role in the MFC control performance. Different works in literature proved that the use of a first-order *Ultra-Local Model* $(v = 1)$ is enough to stabilize unknown dynamics. However, if the unknown dynamics present second-order behavior with small friction coefficients, the use of a first-order *Ultra-Local Model* would be insufficient to stabilize poorly damped dynamics.[29] In light of this, we propose to develop MFC algorithms with a second-order *Ultra-Local Model* $(v = 2)$

$$\ddot{y}_m = F_y + \lambda \cdot u \tag{25}$$

The first step to obtain an estimation of the system dynamics, is to apply the *Laplace Transform* in equation (25), considering F_y as a constant piece-wise function. According to elementary operational calculus we transform equations (25) to (26)

$$s^2 Y_m(s) - s y_m(0) - \dot{y}_m(0) = \frac{F_y}{s} + \lambda U(s) \tag{26}$$

where $Y_m(s)$ and $U(s)$ correspond to the *Laplace transforms* of y_m and u. By differentiating twice the previous equation, we can remove the initial conditions $y_m(0)$ and $\dot{y}_m(0)$

$$2Y_m(s) + 4s\frac{dY_m(s)}{ds} + s^2\frac{d^2Y_m(s)}{ds^2} = \frac{2F_y}{s^3} + \lambda\frac{d^2U(s)}{ds^2} \tag{27}$$

However, the variable s in the time domain corresponds to a derivative term with respect to time, which is sensitive to noise corruptions and could amplify the noise measurement in the output of $\hat{F}_y$. In order to reduce noise in the output estimation, we replace these derivative terms by integral functions ($\frac{1}{s}$) who have robust properties against noise. Thus, multiplying both sides of equation (27) by s^{-3}, we obtain

$$\frac{2Y_m(s)}{s^3} + \frac{4}{s^2}\frac{dY_m(s)}{ds} + \frac{1}{s}\frac{d^2Y_m(s)}{ds^2} = \frac{2F_y}{s^6} + \frac{\lambda}{s^3}\frac{d^2U(s)}{ds^2} \tag{28}$$

Equation (28) can be transferred back to the time domain employing elementary calculus and *Cauchy's formula* to reduce multiple integrals in a simple one

$$\hat{F}_y(t) = \frac{5!}{2T^5}\int_{t-T}^{t}[(T-\sigma)^2 - 4\sigma(T-\sigma) + \sigma^2]y_m(\sigma) - \left[\frac{\lambda}{2}\sigma^2(T-\sigma)^2 u(\sigma)\right]d\sigma \tag{29}$$

From measurements of $y_m(t)$ and $u(t)$ obtained in the last T seconds, the unmodeled dynamics of y and the disturbances are estimated by $\hat{F}_y(t)$ which is updated for each interval of integration $[t-T, t]$. This interval corresponds to the integration window of a receding horizon strategy which results in a trade-off. The idea is to choose small integration windows to calculate the estimation within an acceptable short delay but large enough in order to preserve the low-pass filter properties, whose noise attenuation of $y_m(t)$. Based on such estimator, it is possible to design a robust controller that estimates the system dynamics on-line by a piece-wise function $\hat{F}_y(t)$ periodically updated for each measure of $y_m(t)$ and $u(t)$. According to Figure 5, the MFC closed-loop command is given by

$$u(t) = \underbrace{-\frac{\hat{F}_y(t)}{\lambda}}_{\text{Nonlinear Cancellation}} + \underbrace{\frac{\ddot{y}_{sp}(t) + u_{\mathcal{K}}(t)}{\lambda}}_{\text{Closed-loop tracking}} \tag{30}$$

where $\xi_y(t) = y_m(t) - y_{sp}(t)$ represents the tracking error and $u(t)$ is the closed-loop command of a feedback controller $\mathcal{K}(\xi_y(t))$, usually defined as a proportional (P), proportional-derivative (PD) or even so as proportional-integral-derivative (PID) gains. In this paper, the feedback controller was composed of proportional K_p and derivative K_d gains. We recognize in equation (30) the typical mathematical expression of a nominal control in the flatness-based in which the nonlinear terms $\hat{F}_y(t)$ is added with a closed-loop tracking of a reference trajectory $t \rightarrow y_{sp}(t)$. The error dynamic can be deduced from the combination of equation (30) with equation (25)

$$\ddot{y}_m(t) - \ddot{y}_{sp}(t) = \overbrace{F_y(t) - \hat{F}_y(t)}^{\xi_{F_y}} + K_p\xi_y(t) + K_d\dot{\xi}_y(t) \tag{31}$$

$$\ddot{\xi}_y(t) = \xi_{F_y} + K_p\xi_y(t) + K_d\dot{\xi}_y(t) \tag{32}$$

$$\ddot{\xi}_y(t) - K_d\dot{\xi}_y(t) - K_p\xi_y(t) = \xi_{F_y} \tag{33}$$

Note that, if the error (ξ_{F_y}) between the estimator and the true dynamics is approximately zero during $[t-T, t]$, a simple proportional-derivative controller will be enough to ensure the error convergence to zero because an integration effect is implicitly involved in the MFC algorithm.

MFC design

The MFC closed-loop allows the design of both tracking and regulation performance with distinguished

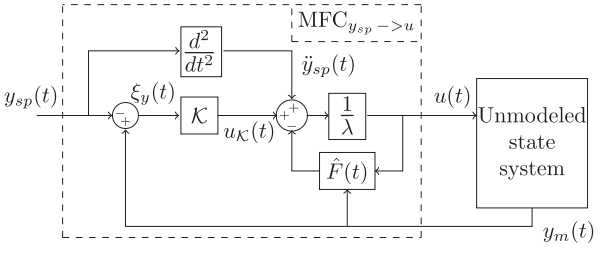


Figure 5. Overview of the model-free control schema.

Table 1. MFC parameters used in the simulations.

States	T_i	λ_i	Kp_i	Kd_i
x	5	25	−0.1225	−0.7
y	10	25	−0.04	−0.4
z	5	20	−0.25	−1
v_{xb}	2	10	−16	−8
v_{yb}	2	70	−7.84	−5.6
v_{zb}	5	2350	−4.6225	−4.3
ϕ	5	300	−4	−4
θ	5	450	−16	−8
ψ	3	1.15	−0.16	−0.8

parameters that can be tuned with little prior knowledge of the system. The following points describe the design methodology used in this work to obtain the MFC parameters presented in Table 1.

1. The proportional-derivative gains (K_p and K_d) have been easily tuned according to classical root locus method. In practice, the MFC estimator provides an accurate estimation of the system ($\xi_{F_y} \approx 0$). Thus, the error dynamics of the closed-loop system can be approximated by a double integrator (33), which can be tuned by pole location approach. In this perspective, we define double real closed-loop poles at $-s_d$, which results the following characteristic polynomial

$$(s + s_d)^2 = s^2 + 2s_d s + {s_d}^2 \tag{34}$$

The feedback controller with these proportional-derivative gains can be identified by neglecting the initial conditions in the Laplace transform of equation (33)

$$\frac{U_{\mathcal{K}}(s)}{\xi_y(s)} = s^2 - K_d s - K_p \tag{35}$$

Therefore, we obtain the following from equations (34) and (35)

$$K_p = -{s_d}^2 \quad \text{with} \quad s_d > 0 \tag{36}$$

$$K_d = -2s_d \quad \text{with} \quad s_d > 0 \tag{37}$$

2. The integration window (T) could be defined with prior information about the noise present in the measured signal (y_m). The choice of the integration window implies some expertise according to a trade-off between fast estimations and effective noise attenuation. For instance, due to the integrator in equation (29) with low-pass filter features, a large integration window provides an effective noise attenuation, but slow estimations with a direct impact on the control-loop responsiveness. On the other hand, small integration windows result in fast estimations with the constraint of estimating noises. In this context, oscillations could be observed in the closed-loop system with high frequency commands (u), which is known as 'chattering'. In this work, we use an invariant observer[44] that smooths the measured signals, allowing the set of small integration windows to estimate the fast dynamics of the DarkO tailsitter MAV while suppressing the oscillations generated by the noises in the closed-loop system.
3. Finally, the constant coefficient (λ) is used to scale the amplitude between the command (u) and the dynamics of ($\ddot{y}_m$). This parameter can be represented as the control effectiveness of the nominal system. Nonetheless, if this parameter is poorly defined or if the actual control effectiveness of the system changes on within a bounded domain, the estimator ($\hat{F}_y$) is able to compensate this bounded discrepancy ensuring the closed-loop stability. A nominal setting of λ can be achieved by calculating the ratio between the command saturation and the maximum allowable value of ($\ddot{y}_m$).

From a practical point of view, the proposed MFC design allows a time-saving approach to stabilize complex dynamic systems. The fact that, the closed-loop system can be approximated by the dynamics of a double integrator system simplifies the control design process of proportional-derivative gains.

Control architecture

Figure 6 shows the main ideas of our control architecture. The block *Trajectory generator* is composed of a state flow algorithm that defines constantly the desired positions (x_{sp}, y_{sp}, z_{sp}) in the inertial coordinate system. These references are taken into account by the *Position control* block and are compared with the respective measures (x_m, y_m, z_m) creating three errors that are minimized by the MFC algorithms in the *Position control* block. These three MFC algorithms in charge of the position tracking, also compute the desired velocity in their respective axes. These reference values which are defined in the inertial coordinate frame are transformed to the body coordinate frame as well as the velocities measurements. Thus, the velocity control $\text{MFC}_{v_{xb}}$ computes the required thrust T_d to reach this desired velocity along $\vec{x_b}$, the block $\text{MFC}_{v_{zb}}$ assures the velocity control along $\vec{z_b}$ and determine the necessary pitch angle θ_{sp} to reach this desired velocity $v_{zb_{sp}}$. Both blocks control their

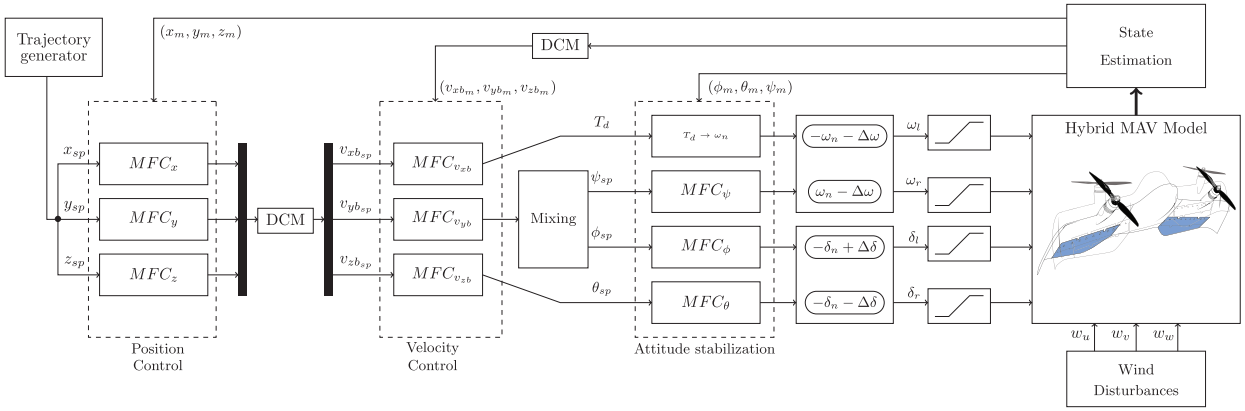


Figure 6. Cascaded MFC architecture designed for tailsitter MAVs. Position control blocks send desired velocities for the velocity control blocks that compute the necessary thrust value as well as the references for attitude stabilization control loop. Based on these desired values, propeller speeds (ω_l, ω_r) and flap deflections (δ_l, δ_r) are defined.
MAV: micro air vehicle; DCM: Direction Cosines Matrix.

respective velocities and define the desired thrust and pitch angle for the entire flight envelope, i.e. hover, transition and forward flight. However, the velocity control along $\vec{y_b}$ is designed depending on the current hybrid MAV flight phase. Therefore, in hover flight, the block $\text{MFC}_{v_{yb}}$ defines the desired yaw angle ψ_{sp} and the block MFC_ψ controls its dynamics through differential-thrust commands creating moments around $\vec{z_b}$ in order to reach the desired velocity along $\vec{y_b}$. In forward flight, this lateral velocity is reached from roll rotations around $\vec{x_b}$. These rotations orient the lift force and the hybrid MAV can perform left-right turns with, respectively, negative and positive roll angles ϕ. The propeller speeds (ω_l, ω_r) are defined by the sum of nominal propeller rotation ω_n with a differential propeller speed Δ_ω which is in charge of the yaw control. The negative sign of ω_n for the left-propeller ω_l is due to the counter-rotation sense. And the flap-deflections (δ_l, δ_r), which are in convention negative for pitch-up, are composed by the sum of symmetrical flap deflection δ_n with anti-symmetrical flap deflections Δ_δ that are respectively the control-input for the pitch angle θ and for the roll angle ϕ.

Flight simulation results

A comprehensive set of flight simulations, discretized at 500 Hz, were performed from MATLAB/Simulink using the tailsitter MAV model described in the 'Simplified tailsitter MAV model' section that is controlled by the proposed MFC architecture, see Figure 6. Our flight simulator is based on the DarkO tailsitter MAV dynamics with sensor measurements corrupted by Gaussian white noises, whose standard deviations can be found in literature.[45] The MFC parameters, i.e. λ_i, T_i, Kp_i and Kd_i, were tuned for the entire flight envelope of the DarkO with constant values for all flight simulations. In order to evaluate our control algorithm, we have introduced external perturbations such as wind disturbances during these flights. The results provide a straightforward way to validate the methodological principles presented in this article as well as to evaluate the designed MFC parameters, and to establish a conclusion regarding MFC benefits in both theoretical and practical contexts. The flight simulations are presented in a series of case studies in order to analyze separately each flight domain of the DarkO, such as hovering, transitioning and forward flights.

Hovering flight

In hovering flight, we analyze the velocity and attitude controller's ability to recover the MAV from different unstable initial condition points. Also, we present an average frequency content of yaw and pitch angle signals using the Fast Fourier Transform (FFT) algorithm over the entire time that the signals were acquired. In addition, we present two position tracking missions in hovering flight, and we verify the interaction between the position, velocity and attitude control blocks.

Initial condition analysis. The initial conditions for pitch angle and for forward speed during the hovering flight (θ_{ic} and $V_{x_{ic}}$), follow a normal distribution law according to equations (38) and (39).

$$\theta_{ic} \sim \mathcal{N}\left(\frac{\pi}{2}, \left(\frac{\pi}{6}\right)^2\right) \tag{38}$$

$$V_{x_{ic}} \sim \mathcal{N}\left(0, \left(\frac{5}{3}\right)^2\right) \tag{39}$$

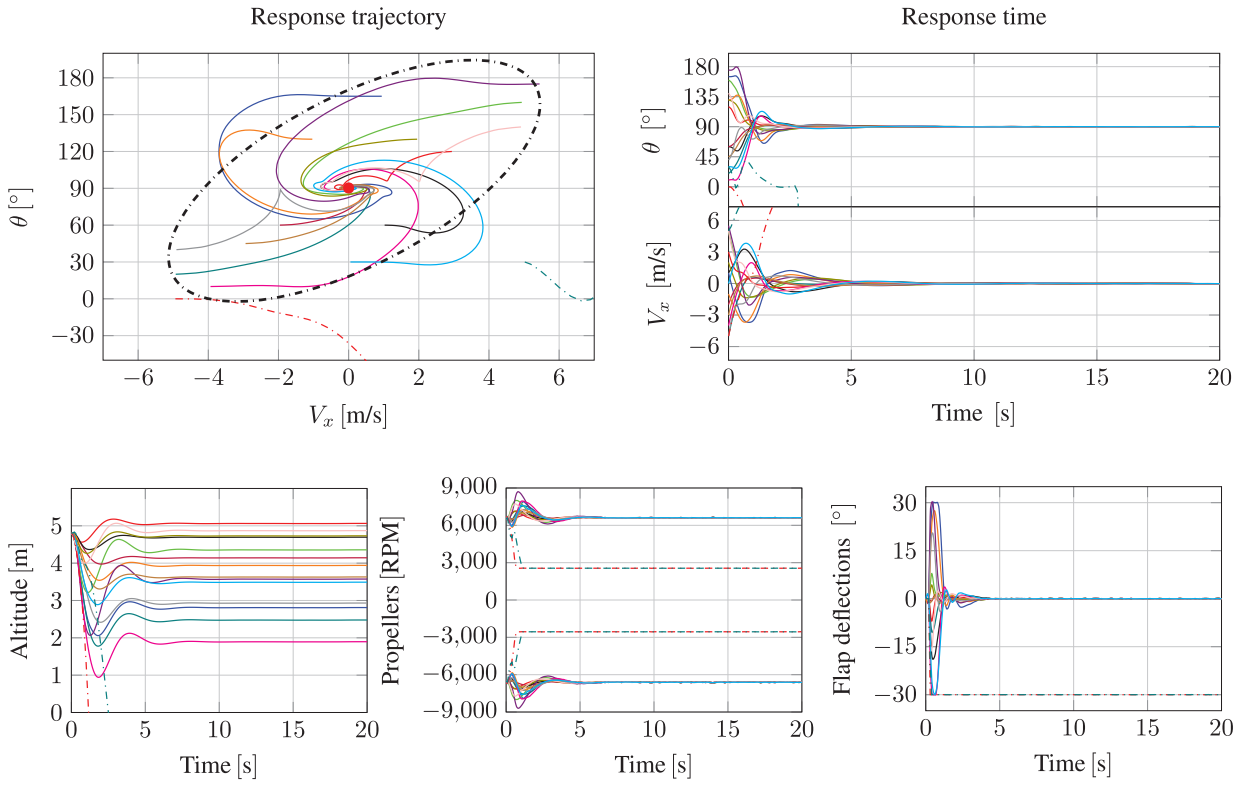


Figure 7. Initial pitch angle and forward speed condition analysis during hovering flight phase without wind disturbances. Forward speed setpoint equals to 0 m/s, the MFC architecture computes the pitch angle setpoint equals to 90° in order to reach the stationary flight.

The stability boundary presented in Figure 7, was empirically defined by evaluating all recovery trajectories from initial conditions to the desired setpoint. The desired setpoint corresponds to a stationary flight in the vertical position, respectively, 0 m/s for the forward speed and 90° for the pitch angle. Basically, three classes of trajectories were distinguished during these simulations. The first one combines trajectories with initial pitching angles larger than 90° with positive initial conditions for forward speeds. Likewise, trajectories with initial pitching angles smaller than 90° and negative initial conditions for forward speeds are also included in this class. The peculiarity of these trajectories is that, both converge directly to the desired equilibrium setpoint with small oscillations in the response time. This can be explained by the fact that, for initial pitching angles larger than 90°, the thrust vector is already well-oriented and it can be increased in order to decelerate the initial positive forward speeds. This thrust vector is increased from increments of the propeller rotations, which improves the flap effectiveness creating a powerful pitch moment that can easily align the attitude of the hybrid MAV in the right direction, towards the attitude setpoint. The same reasoning can be done for initial pitching angles smaller than 90° with negative forward speeds. In this initial flight condition and orientation, the controller generates the thrust vector in order to increase the forward speed resulting in an effective pitch moment which also steer the hybrid MAV towards the setpoint. The second class of trajectories is composed by all initial pitching angles smaller than 90° with positive initial forward speeds and by all initial pitching angles larger than 90° with negative initial forward speeds. These trajectories diverge at the beginning of the simulation. The thrust vector, in these flight orientations, is unable to generate an opposing force to decelerate the initial forward speed to zero. The only force opposing to the movement is the drag force. By increasing the pitch angle, in this case the angle of attack, the hybrid MAV generates more drag and can reach the forward speed setpoint. For extreme cases, within the stability boundary, we can observe flap saturation which justifies the shape of the concerned trajectories with overshoots and undershoots. By analyzing the altitude results, we can mention that the position control is not activated. However, we can observe that the altitude is stabilized at given values according to the velocity control block which cancels the vertical velocity component. The MFC can theoretically ensure a

stable flight for all initial points inside the boundary, with more or less oscillations, according to the initial conditions. Otherwise, the hybrid MAV performs an unstable flight, as shown by the two particular initial points outside the stability boundary corresponding to the third class of trajectories in this simulation.

FFT analysis. This analysis focuses on the MFC tuning problem. Usually, the flight controller parameters are adjusted according to a setpoint trajectory and with trim points in a respective flight condition. However, hybrid MAV covers different flight domains which would imply a variety of setpoint trajectories with different frequencies. Thus, we analyze the entire bandwidth of frequencies corresponding to the yaw and the pitch angle during the hovering flight. And, we compare its setpoint trajectory spectrum with its measured spectrum in order to evaluate the designed MFC parameters. We excite the attitude dynamics adequately in order to capture the important frequencies by varying the velocity setpoint along the $y_b - axis$ and the velocity setpoint along the $z_b - axis$. According to Figure 6, the block MFC_{v_y} generates, in hovering flight, the setpoint to the yaw angle ψ_{sp} and the block MFC_{v_z} the setpoint to the pitch angle θ_{sp}. Figure 8 shows the comparison between the desired yaw angle and its respective measured signal in both time and frequency domains. High precision tracking for frequencies up to 4 rad/s is observed which means that the controller is able to track, with high precision, yaw setpoint variations up to 285 degrees per second ($^\circ$/s). Furthermore, the tuned yaw control parameters present a reasonable trade-off to track low and high frequencies that compose its bandwidth. The results of the pitch angle presented in Figure 9, shows an effective tracking over its entire frequency spectrum. In addition, for high frequencies, the controller filters the references providing a smooth pitch output, but with an offset between the signals creating a small error.

Hovering flight missions. The main objective of the first flight simulation in hovering mode, see Figure 10, is the study of wind influence in the position tracking, for the following desired positions

$$\begin{aligned} x_{sp} &= 0, \forall t \\ y_{sp} &= 0, \forall t \\ z_{sp} &= \begin{cases} 10, & t \in [0; 155]s \\ 0, & t > 155s \end{cases} \end{aligned}$$

During this flight mode (**#Flight 1**), the hybrid MAV is more susceptible to aerodynamics disturbances. We can explain this by the fact that, in the vertical position, the wind gust along the $x_i - axis$, respectively along the $z_b - axis$, is in contact with the total reference wing area generating a considerable drag force. Also, the hybrid MAV is not able to compensate this force in the vertical position. That is why, the transition is performed and the drag force created by the wind can be compensated by the thrust in order to ensure the position tracking. The thrust used to reject this

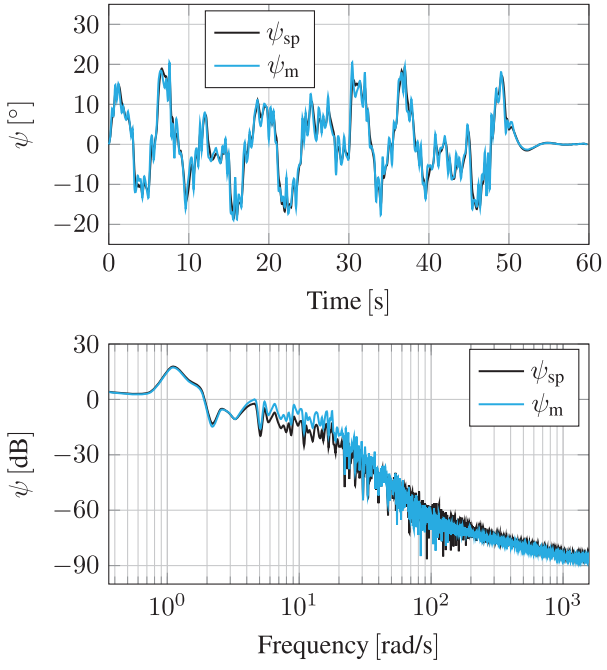


Figure 8. Frequency analysis of the yaw angle in hover flight.

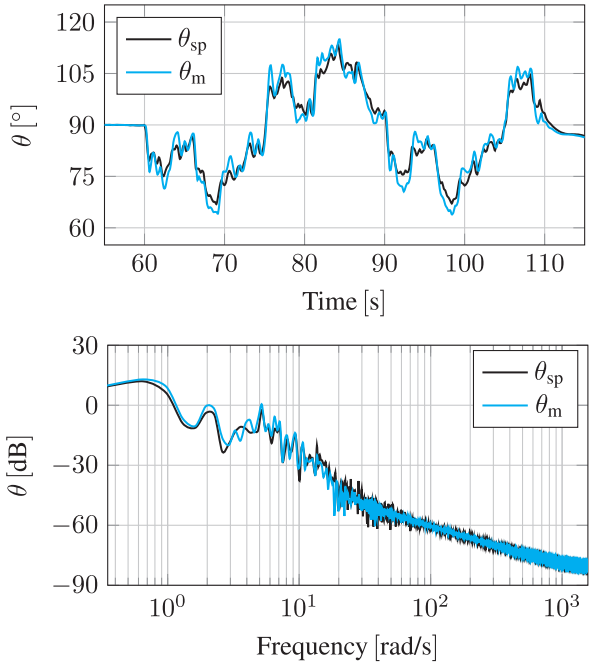


Figure 9. Frequency analysis of the pitch angle in hover flight.

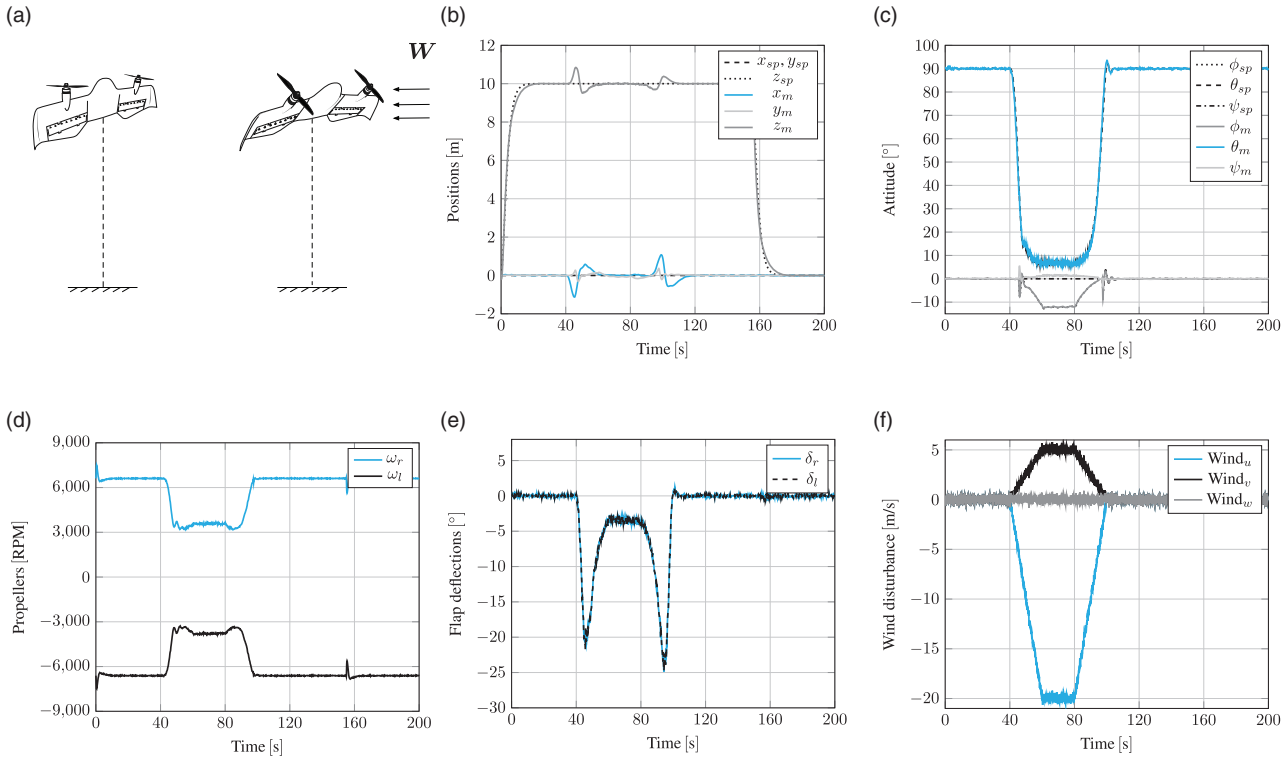


Figure 10. (**#Flight 1**) – Vertical take-off and transition flight to assure position tracking during high crosswind. On the top, from left to right: simulation illustration, positions in the inertial coordinate frame and attitude. On the bottom: propeller speeds ($\omega_l < 0$ and $\omega_r > 0$) due to counter-rotation sense, flap deflections (δ_l and δ_r) convention negative for pitch-up, and wind disturbance.

perturbation can be seen in Figure 10(d). And the wind from east with a magnitude of 5 m/s, see Figure 10(f), also produces a side force in the $y_b - axis$. This force is compensated by orienting the lift force with a symmetrical rotation around the $x_b - axis$, corresponding to the negative roll angle described in Figure 10(c).

In the second flight simulation, we impose a circular setpoint path (**#Flight 2**) in order to validate the interaction between all control blocks in the proposed control architecture. The following equations define the desired trajectories (x_{sp}, y_{sp}, z_{sp})

$$x_{sp} = \begin{cases} 0, & t < 30s \\ x_c + r\,cos\left(\frac{2\pi}{40}t\right), & t \in [30;130]s \\ 1, & t > 130s \end{cases}$$

$$y_{sp} = \begin{cases} 0, & t < 30s \\ y_c + r\,sin\left(\frac{2\pi}{40}t\right), & t \in [30;130]s \\ 5, & t > 130s \end{cases}$$

$$z_{sp} = \begin{cases} 10, & t \in [0;155]s \\ 0, & t > 155s \end{cases}$$

where x_c and y_c correspond to the center of the circle and r is its radius. This maneuver requires the hybrid MAV to fly along a circular trajectory while constantly pointing its nose towards the exact center of the circle. Accurate position, velocity and especially yaw angle control are needed to accurately follow the desired flight plan with the desired attitude. Figure 11 shows the simulation results.

Remark (Conclusion hovering flight phase). *In hovering flight simulations, the MFC architecture has shown the capability to recover the tailsitter MAV from a large range of initial conditions for both pitch angle and forward speed, thereby validating the interactions between attitude and velocity control blocks. The disturbances that deteriorate the controlled output signal, are estimated and annulled by the controller providing robust disturbance rejections in order to track a desired position. For strong wind disturbances, the tailsitter MAV performs a smooth transitioning flight ensuring position tracking. Indeed, the FFT analysis validated the designed MFC parameters for a wide attitude frequency spectrum.*

Transitioning flight

The transitioning flight simulations were examined in two parts. In the first one, similar to the hovering flight,

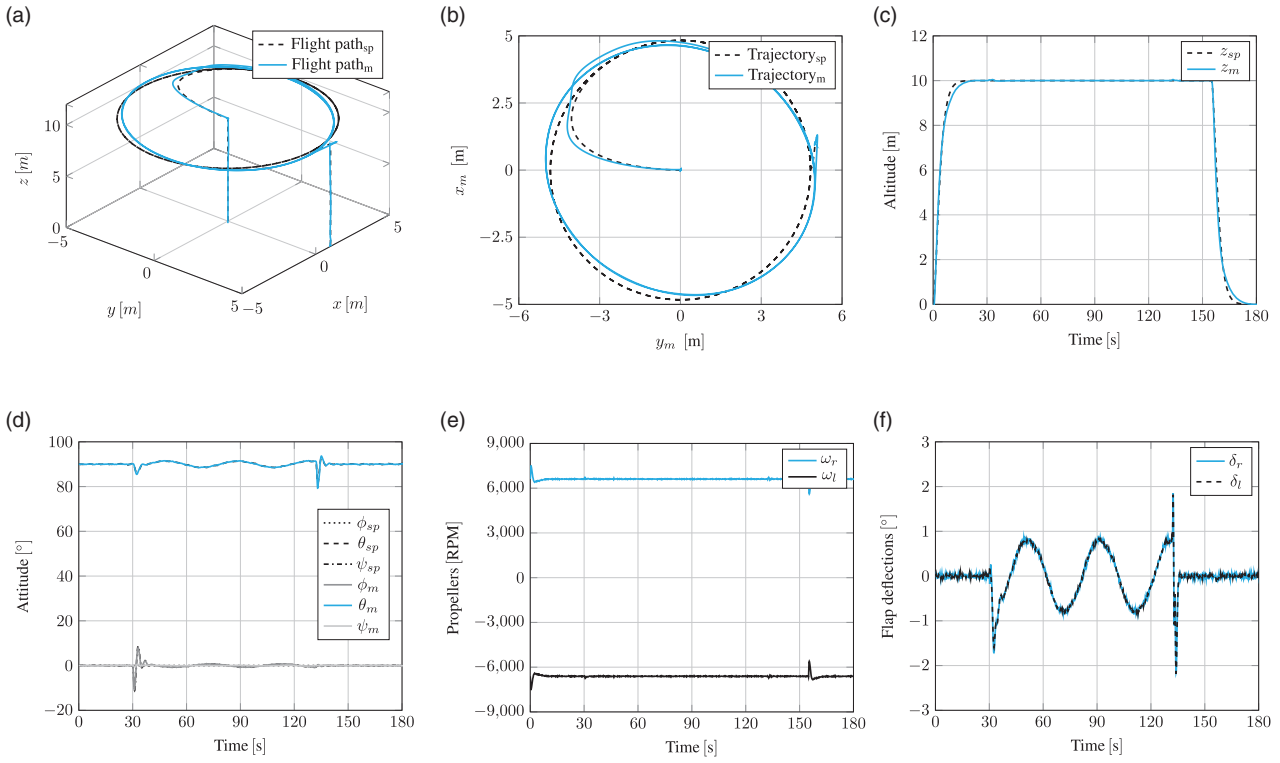


Figure 11. (**#Flight 2**) – Circular position tracking in hover flight mode. On the top, from left to right: the 3D flight path, North and East positions and altitude. On the bottom: attitude, propeller speeds and flap deflections.

we analyze the velocity and attitude controller's ability to recover the MAV from different unstable initial conditions to the desired stable setpoint. The second case study presents variations of nominal hybrid UAV parameters in flight at different pitch angles in order to evaluate the MFC adaptive properties during the forward-to-hover transition.

Initial condition analysis. In this case study, we define a forward speed setpoint of 5 m/s and the MFC architecture computes a pitch angle setpoint of around 45°. The desired forward speed setpoint was chosen to prove, by flight simulations without predefined gains or gain scheduling methods, that the proposed control architecture is able to stabilize the tailsitter MAV in a critical flight domain corresponding to stall region where the aircraft flies at low forward speed and high angle of attack. The initial conditions during the transitioning flight analysis (θ_{ic} and $V_{x_{ic}}$), are defined from a normal distribution law given by the following equations (40) and (41).

$$\theta_{ic} \sim \mathcal{N}\left(\frac{\pi}{4}, 30^2\right) \tag{40}$$

$$V_{x_{ic}} \sim \mathcal{N}(5, 2^2) \tag{41}$$

The empirically defined stability boundary, for initial conditions in transitioning flight, is presented in Figure 12. The three classes of trajectories discussed in the hovering flight analysis, can be also observed in this case study. These trajectories have a slower convergence time with respect to the trajectories in hovering flight domain. Flap saturation affects the response time, but the main reason for the slower convergence time, in the transitioning flight domain, is the difficulty to decelerate the tailsitter MAV which depends on only of the drag force. For these initial conditions, the tailsitter MAV was not controlled in position allowing a supplementary degree of freedom to recover the stable attitude setpoint. During the transitional regime, that corresponds to the trajectory from the initial conditions to the setpoints, the tailsitter MAV loses altitude because the initial condition for both pitch angle and forward speed precludes the production of lift force and the thrust orientation is not adequate to compensate the weight of the tailsitter MAV. Thus, fast attitude stabilization is crucial to steer the thrust and bring the tailsitter MAV back to safe flight conditions.

Parameter-varying analysis. In this analysis, we evaluate the altitude tracking and the attitude stabilization, more precisely, the pitch angle stabilization by imposing variations of mass and inertia at different points in

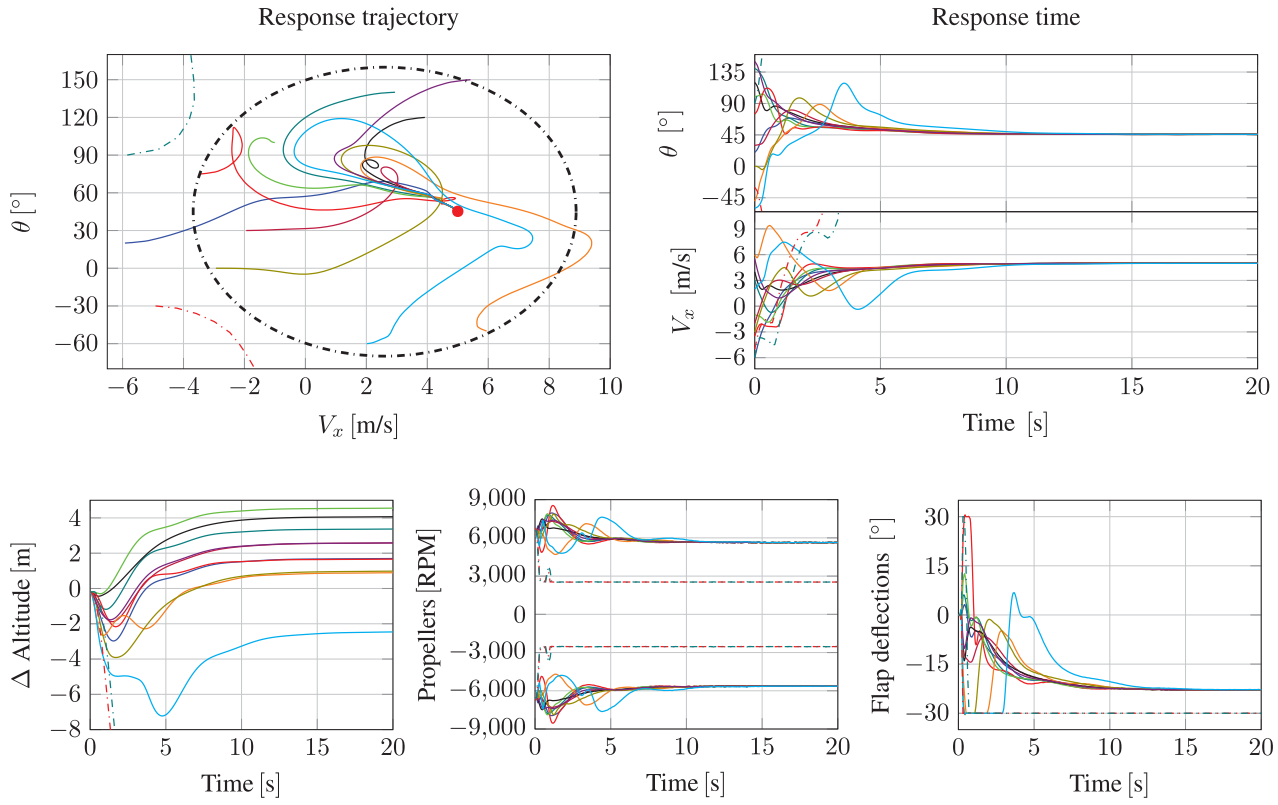


Figure 12. Initial pitch angle and forward speed condition analysis during the transitioning flight phase without wind disturbances. Forward speed setpoint equals to 5 m/s, the MFC architecture computes the pitch angle setpoint approximately equals to 45°.

the pitch angle trajectory during the forward-to-hover transition. For each point in which the variations occur, we compute the standard deviation between the altitude setpoint and its measurement. Figure 13 shows a typical pitch angle response time for the forward-to-hover transition with the nominal DarkO parameters. The altitude behavior and its standard deviation values computed for different mass and inertia values are also presented. We impose a maximum mass and inertia variation of around 45% of the nominal DarkO parameters. This study concludes that, the DarkO is less robust to variations of mass and inertia when it occurs between 20° and 40° of pitch angle. However, the impact of mass and inertia variations on altitude tracking remains very low with a maximum standard deviation of 0.3 m. The proposed control approach is able to stabilize the forward-to-hover flight transition with little prior knowledge of the tailsitter MAV. By using the estimator ($\hat{F}$) in the closed loop, any impact on the tailsitter MAV dynamics caused by parametric variations are estimated and immediately compensated in order to reach the altitude setpoint trajectory previously imposed.

Remark ((Conclusion transitioning flight phase)). *Fast changing of aerodynamic forces and moments present in this critical flight domain have been countered by the proposed control architecture. The tailsitter MAV is stabilized in a critical attitude setpoint from different initial conditions. Further, the parameter-varying analysis highlighted the promising adaptive properties of the proposed control technique.*

Forward flight

The last phase of flight studied corresponds to the forward flight. Given that, the MFC parameters are tuned for the entire flight envelope without any type of gain scheduled and the hybrid MAV dynamics change between the flight phases, we compute the FFT to the roll and the pitch angles in order to compare the frequency control performance with the previous results in hovering flight. In addition to this analysis, we present a full flight simulation exploring all hybrid MAV flight phases, with a major focus on forward flight, in which the hybrid MAV performs a position tracking.

FFT analysis. In forward flight, the roll setpoint ϕ_{sp} is generated from the velocity control block along the $y_b - axis$. This velocity is excited in order to create different setpoint values and frequencies to the roll angle. The roll tracking results in both time and frequency

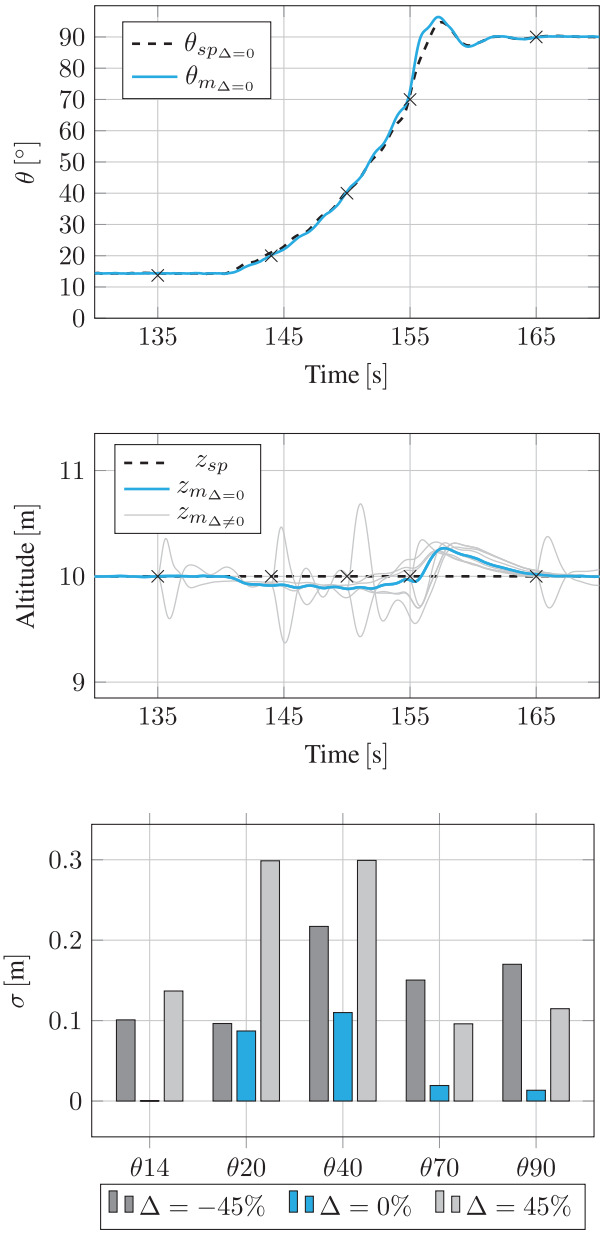


Figure 13. Parameter variation analysis for different points in the forward-to-hover transition. The black crosses in altitude and pitch angle trajectories indicate the points in which the parameters were changed. Δ represents the variation of nominal mass and inertia in percentage. The standard deviation between the altitude setpoint and its measurements is denoted by σ.

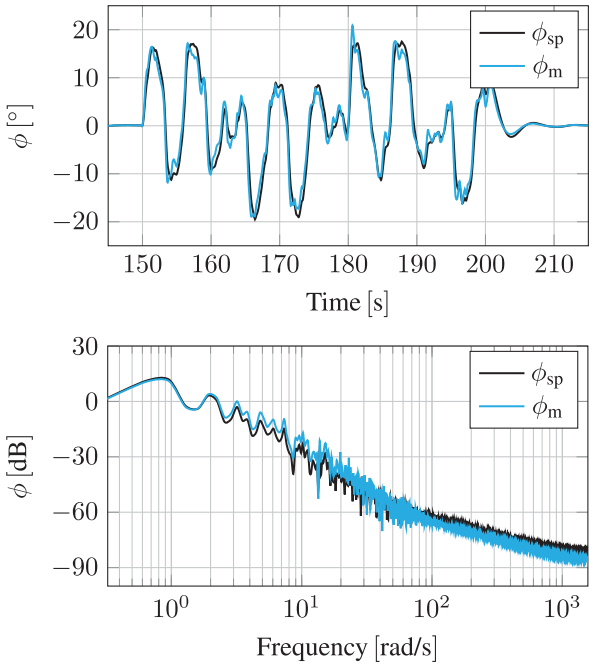


Figure 14. Frequency analysis of the roll angle in forward flight.

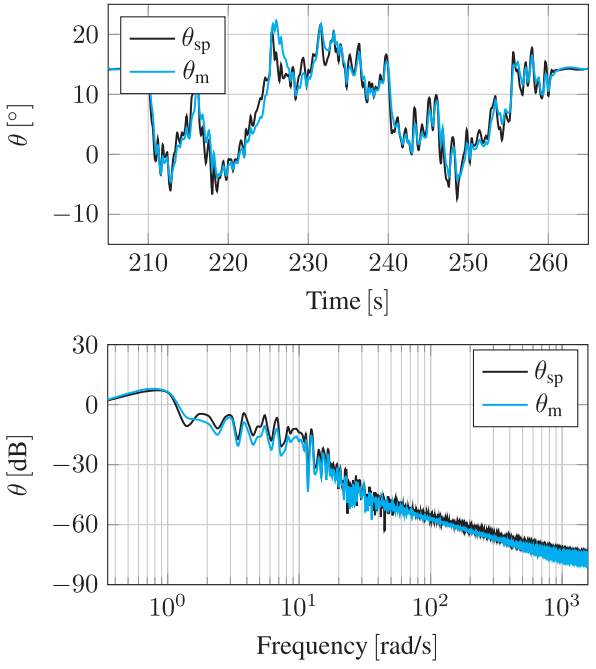


Figure 15. Frequency analysis of the pitch angle in forward flight.

domains are presented in Figure 14. The proposed controller provides a high quality tracking up to 3 rad/s which is equal to 170 (°/s). An offset between the roll setpoint trajectory and the roll measurement is observed at high frequencies. However, in this frequency range, the signals are almost negligible, given their respective attenuation in decibels.

Pitch angle results are presented in Figure 15. We quantify a maximum pitch tracking error of 1.58 (°) for pitch angle setpoints varying between 1 and 10 rad/s, which represent 57 and 573 (°/s). Overall, the FFT analysis revealed, in hovering and forward flight, the promising performance of MFC for attitude tracking. Further, this analysis shows that the MFC parameters were well-adjusted considering the trade-off between

the quality of attitude stabilization with delays and noises in the control loop.

Forward flight mission. A complete flight mission (#**Flight 3**) is presented in Figure 16 in which we evaluate all hybrid MAV flight capabilities through a vertical take-off from 0 to 10 m of altitude followed by the hover-to-forward transition with a position tracking in the *xy – plane* and an altitude change in forward flight. Then, the forward-to-hover transition is performed with a position tracking in hovering flight. The flight simulation ends with a vertical landing. The complete 3D flight path is presented in Figure 16(a). The controller assures the position tracking during the entire mission. As we can see in Figure 16(b), the altitude presents small oscillations at 45 and 165 s of simulation which is acceptable for this MAV class. These oscillations are due to the fast variations of aerodynamics forces and moments that occur during the transition flight phases where the pitch angle changes resulting in significant variations in the angle of attack, see Figure 16(d). In the same figure, between 45 and 90 s of simulation, we can see the roll dynamics to reach the desired east position in forward flight. Similarly, between 180 and 215 s of simulation, the yaw behavior to reach the east position in hovering flight. Figure 16(c) presents the velocities in the body coordinate system and the actuator dynamics, respectively, the propeller rotations and the flap deflections are shown in Figure 16(e) and (f).

Remark ((Conclusion forward flight)). *We confirm in this subsection that, the proposed MFC architecture also ensures the position tracking, velocity control and attitude stabilization in forward flight. With the FFT analysis, we show the attitude control performance for a large range of frequencies. Furthermore, we validate the interactions between each control block independently of the hybrid MAV attitude orientation that covers its entire flight envelope.*

Flight tests

In this section, we present real-world flight tests to compare the MFC attitude stabilization performance to that of the INDI controller in indoor flight conditions. For more details about the INDI, we refer the interested reader to literature.[25,46] Both controllers were tested using the Paparazzi Open Source Autopilot System.[47] The methodology used during the flight tests to define the DarkO's attitude setpoints are based on four steps. First, with an RC transmitter, the security pilot imposes slow yaw setpoints generating lateral motions in the system. Then, slow pitch

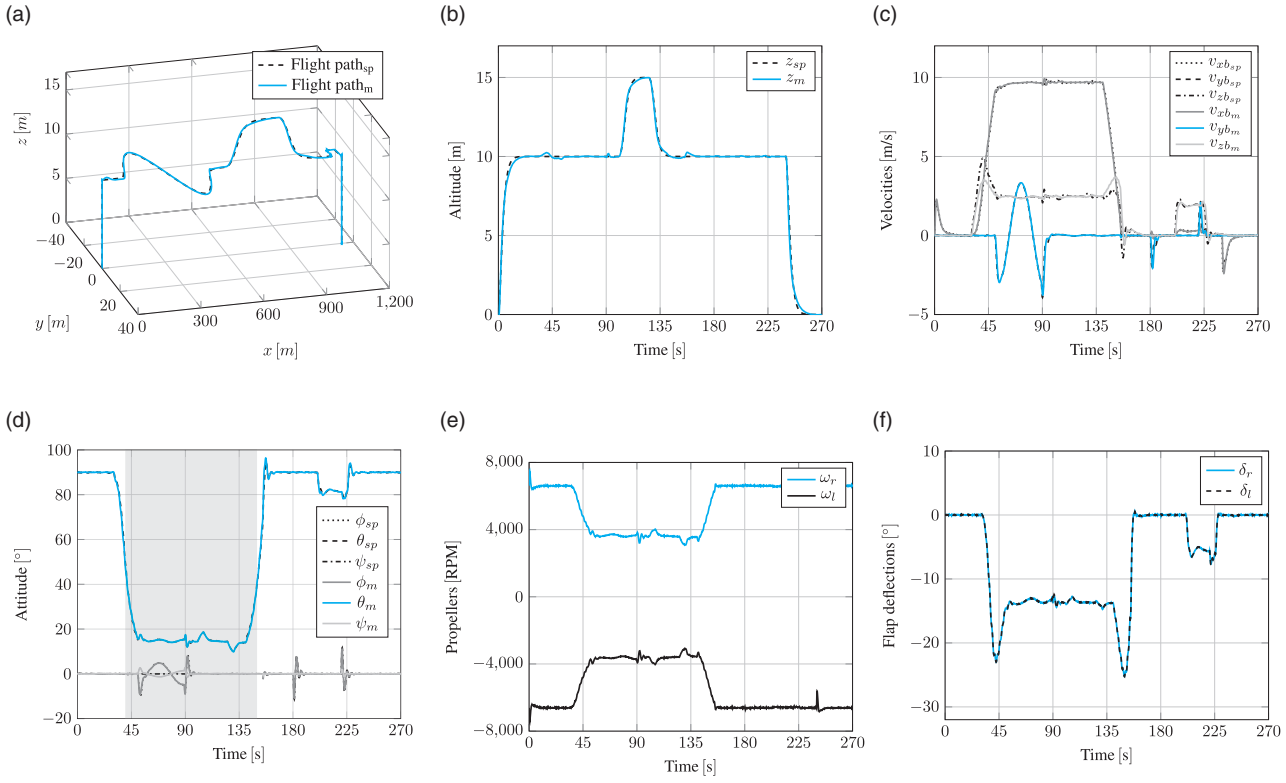


Figure 16. (**#Flight 3**) – Entire flight envelope simulation in relatively calm flight conditions. On the top, from left to right: the 3D flight path, altitude and velocities in the body coordinate system. On the bottom: attitude, propeller speeds and flap deflections.

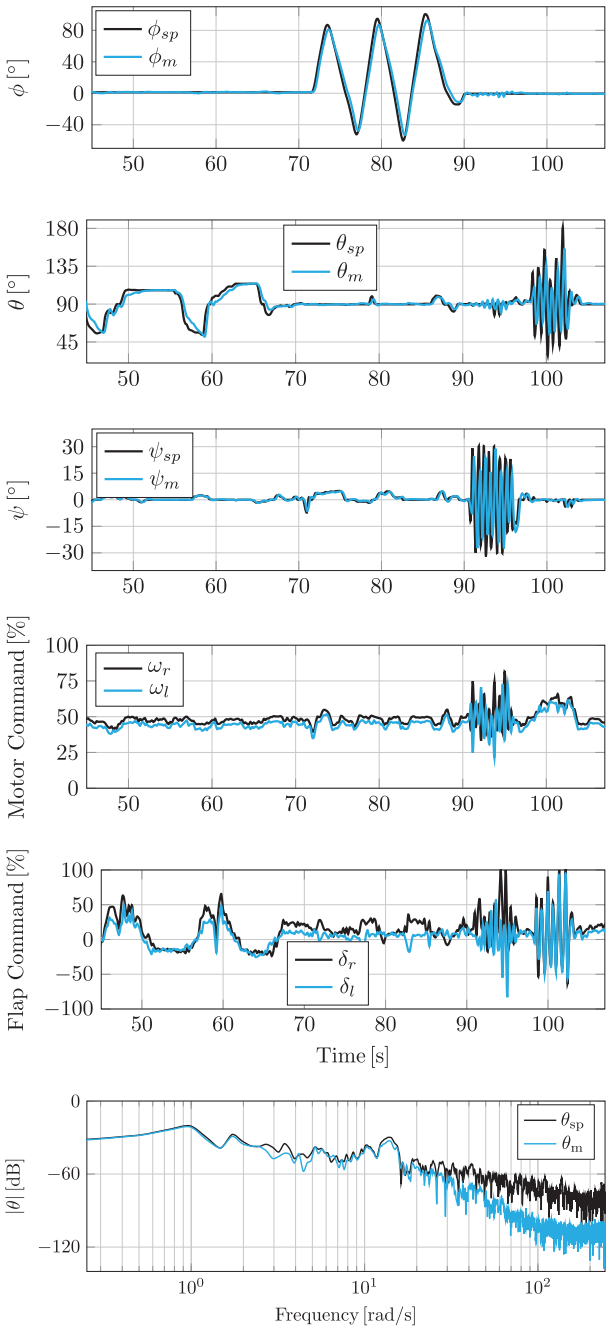


Figure 17. MFC attitude stabilization – nominal DarkO.

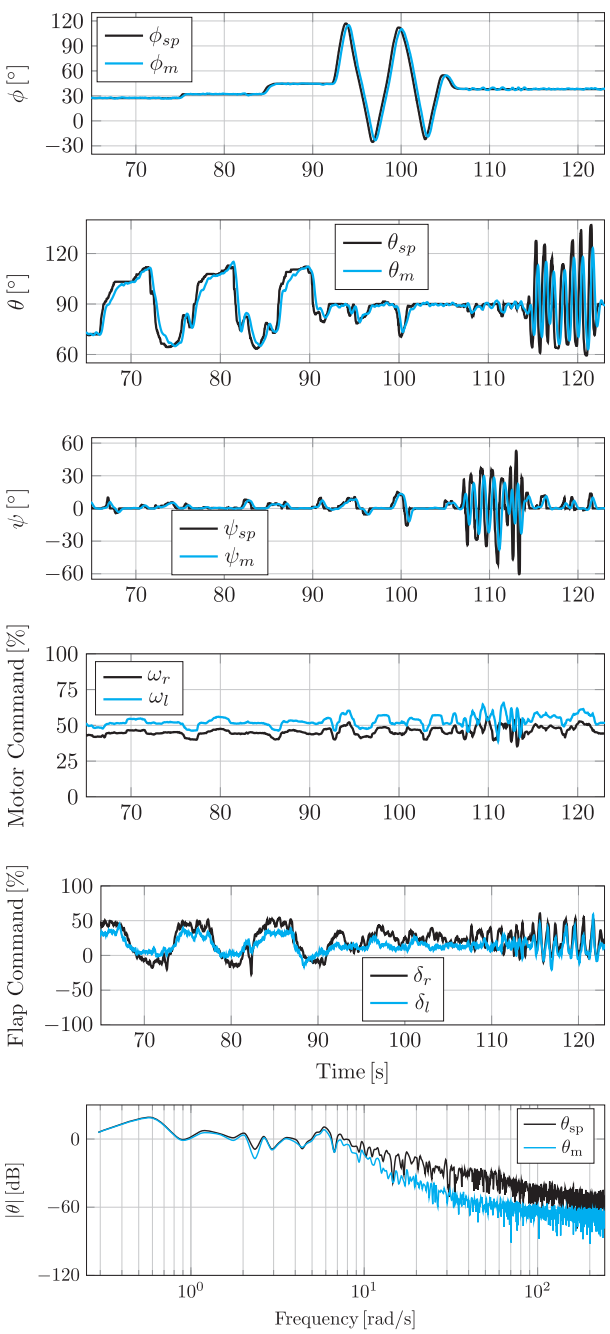


Figure 18. INDI attitude stabilization – nominal DarkO.

setpoints generate forward and backward movements according to positive and negative pitch setpoints, respectively. Then, slow roll setpoints which define the heading of the system. Finally, the pilot imposes fast yaw and pitch setpoints to evaluate the response of the system for high frequency attitude setpoints. Two flight test cases were conducted in indoor environment comparing MFC to INDI controllers. In the first case, both controllers stabilize the DarkO in its nominal configuration, i.e. wings and control surfaces are attached correctly. In the second case, the wingtips and half of the control surface are removed, and additionally the propulsion system has been modified by using a different set of propellers. The nominal components of the DarkO were changed to evaluate the adaptive properties of both controllers. The attitude stabilization results performed by MFC and INDI with the nominal DarkO, are presented in the Figures 17 and 18, respectively. Figures 19 and 20 show the MFC and INDI attitude stabilization performances

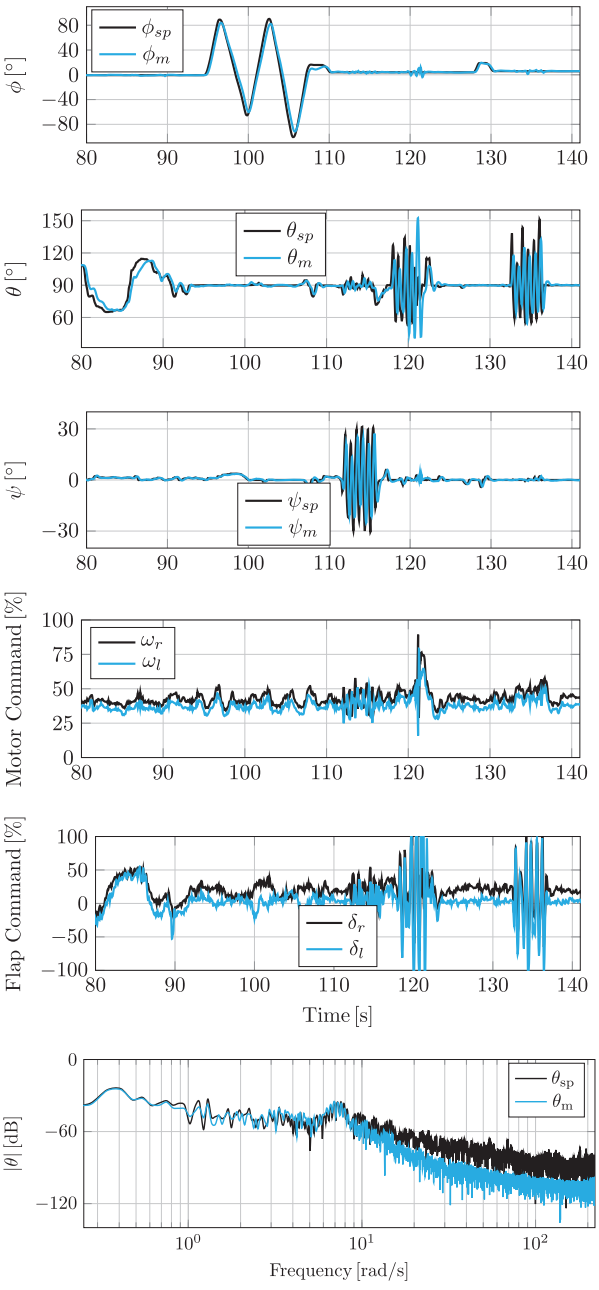


Figure 19. MFC attitude stabilization – modified DarkO.

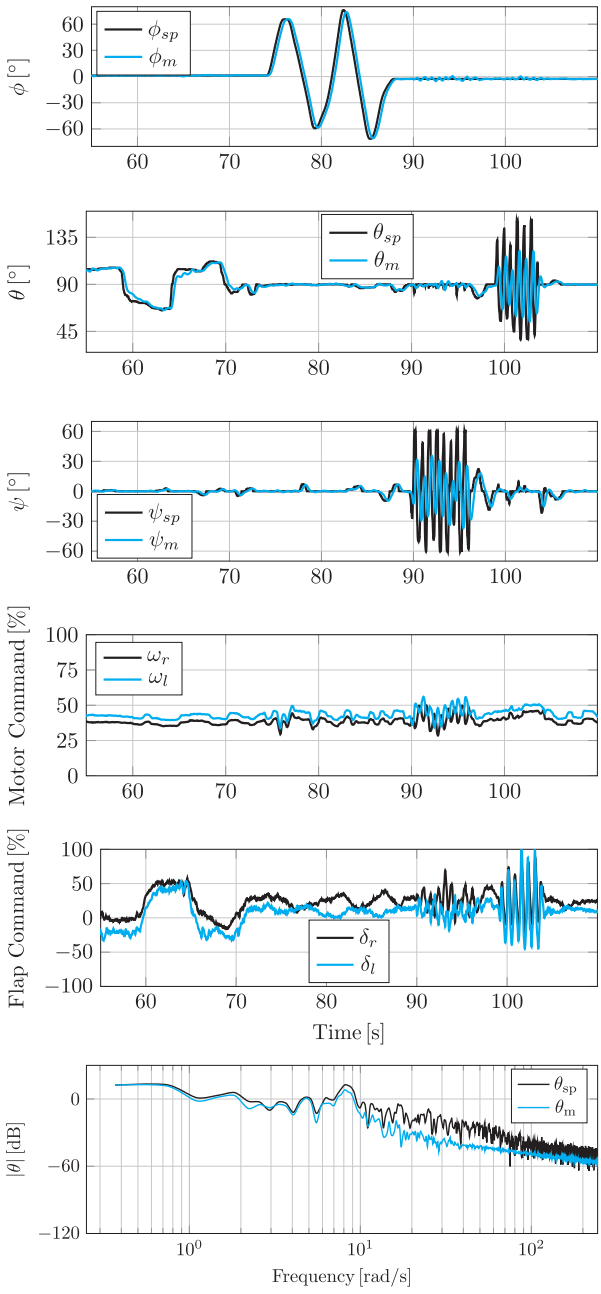


Figure 20. INDI attitude stabilization – modified DarkO.

for the modified DarkO configuration, see Figure 21. It is difficult to analyze graphically each controller in the time domain, because of their different setpoint trajectories. For this reason, we investigated their control performance in the frequency domain by calculating the FFT of the pitch angle, which is the dynamics most affected by a loss of control surface effectiveness. We observe a better tracking performance with a larger frequency spectrum for the MFC (20 rad/s) when compared to that of the INDI (7 rad/s) for the nominal flight test. Both controllers stabilized the modified DarkO, showing their adaptive control properties. The present study concludes that MFC and INDI provide satisfactory performance for hovering and transitioning flight domains in indoor flight conditions. These results suggested a more in-depth analysis to evaluate the performance of both controllers for the entire flight envelope of the DarkO, in particular during forward flights in outdoor environment.

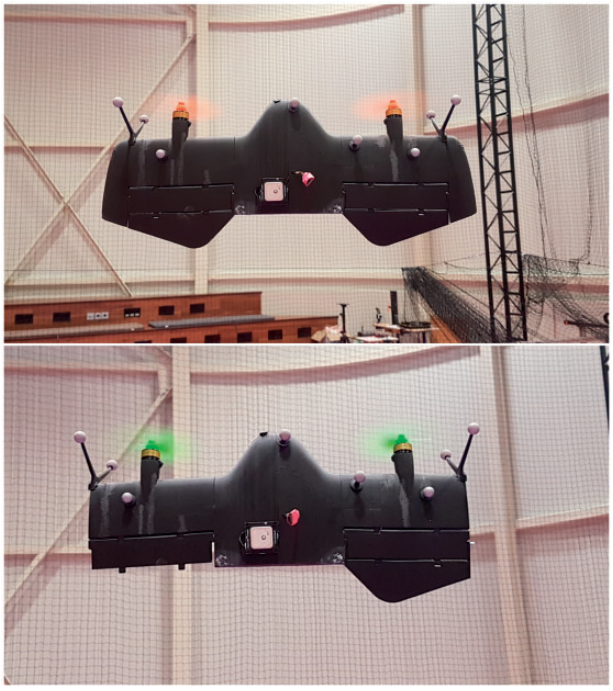


Figure 21. Tailsitter MAV configurations used during flight tests. At the top, DarkO with nominal wings, control surfaces and two-blade propellers. At the bottom, DarkO has been modified by removing its wingtips, half of its control surface and three-blade propellers were used.

Table 2. DarkO MAV parameters.

Parameters	Values	SI units
Mass (m)	0.492	(kg)
Mean chord (c)	0.13	(m)
Wingspan (b)	0.55	(m)
Wing area (S)	0.0743	(m^2)
J_{xx}	0.0070	(kg m^2)
J_{yy}	0.0028	(kg m^2)
J_{zz}	0.0061	(kg m^2)
J_P	5.1116e-06	(kg m^2)
k_f	5.13e-6	(kg m)
k_m	2.64e-7	(kg m^2)
C_{d0}	0.025	No units
C_{y0}	0.1	No units
C_{l_p}	0.2792	No units
C_{l_q}	0.0	No units
C_{l_r}	0.1145	No units
C_{m_p}	0.0	No units
C_{m_q}	1.2715	No units
C_{m_r}	0.0	No units
C_{n_p}	0.081	No units
C_{n_q}	0.0	No units
C_{n_r}	0.0039	No units
p_{p_x}	0.065	m
p_{p_y}	0.155	m
p_{p_z}	0.0	m
p_{a_x}	0.0	m
p_{a_y}	0.155	m
p_{a_z}	0.0	m
ξ_f	0.85	No units
ξ_m	0.55	No units

Discussion and conclusion

The main objective of this study is to show the easy implementation of the MFC algorithm to different hybrid MAV platforms. We have presented the development of a full control architecture based on MFC techniques, applied to MAV with transitioning flight capabilities. Numerical flight simulations were performed in order to validate the interactions between each control block for different flight domains covering the entire tailsitter MAV flight envelope. Attitude control loop performance was examined in frequency domain during the hovering and the forward flight. The FFT results demonstrated high tracking performance for most of the attitude bandwidth. As a critical point, during forward-to-hover transition, we have investigated the adaptive properties of the controller by varying the parameters of the tailsitter MAV during flight. MFC algorithms estimated and rejected the variations of 45% of the nominal parameters providing a stable transitioning flight. The velocity control performance has also been investigated simultaneously with the attitude control block in hovering and transitioning flights for different unstable initial conditions. Both control blocks are able to stabilize the tailsitter MAV from a variety of initial pitch angles and initial forward-speeds recovering the MAV to stable equilibrium points. The proposed control approach provides high performance position tracking, velocity control and attitude stabilization without gain scheduling method and by using only little prior knowledge of the tailsitter MAV. Furthermore, the MFC attitude stabilization performance, its real time estimation and its adaptive properties have been validated in real-world flight conditions. In addition, comparative indoor flight tests between MFC and INDI have been conducted. However, it has been realized that in order to come to a conclusion between the performance of the two controllers, additional flight experiments have to be performed. In particular, during the forward flight phase at outdoor environment so that the disturbance rejection properties of each control approach can be compared and evaluated properly.

Future work will include additional flight tests with different MAV configurations with a wide variety of design parameters. We would also like to investigate if a proof of stability can be established, analyzing the adaptation properties of the MFC estimator in the closed-loop system.

DarkO MAV parameters

The DarkO hybrid MAV's parameters used in this paper for all flight simulations, are presented in Table 2.

Declaration of conflicting interests

The author(s) declared no potential conflicts of interest with respect to the research, authorship, and/or publication of this article.

Funding

The author(s) received no financial support for the research, authorship, and/or publication of this article.

ORCID iD

Jacson MO Barth https://orcid.org/0000-0001-7132-2929

References

1. Santos MA, Cardoso DN, Rego BS, et al. A discrete robust adaptive control of a tilt-rotor UAV for an enlarged flight envelope. In: *IEEE 56th annual conference on decision and control (CDC)*, Melbourne, Australia, 12–15 December 2017. pp.5208–5214.
2. Hartmann P, Meyer C and Moormann D. Unified velocity control and flight state transition of unmanned tilt-wing aircraft. *J Guid Control Dyn* 2017; 40: 1348–1359.
3. Gu H, Lyu X, Li Z, et al. Development and experimental verification of a hybrid vertical take-off and landing (VTOL) unmanned aerial vehicle (UAV). In: *International conference on unmanned aircraft systems (ICUAS)*, Miami, FL, USA, 13–16 June 2017, pp. 160–169.
4. Flores A, Montes de Oca A and Flores G. A simple controller for the transition maneuver of a tail-sitter drone. In: *IEEE conference on decision and control (CDC)*, Miami Beach, FL, USA, 17–19 December 2018, pp. 4277–4281.
5. Chinwicharnam K, Gomez Ariza D, Moschetta J-M, et al. Aerodynamic characteristics of a low aspect ratio wing and propeller interaction for a tilt-body MAV. *Int J Micro Air Veh* 2013; 5: 245–260.
6. Bronz M, Smeur EJJ, de Marina HG, et al. Development of a fixed-wing mini UAV with transitioning flight capability. In: *35th AIAA applied aerodynamics conference, AIAA AVIATION forum*, Denver, CO, USA, 6 July 2017.
7. Argyle ME, Beard RW and Morris S. The vertical bat tailsitter: dynamic model and control architecture. In: *American control conference* (*ACC*), Washington, DC, USA, 7 June 2013, pp.806–811.
8. Forshaw JL, Lappas VJ and Briggs P. Transitional control architecture and methodology for a twin rotor tail-sitter. *J Guid Control Dyn* 2014; 37: 1289–1298.
9. Matsumoto T, Kita K, Suzuki R, et al. A hovering control strategy for a tail-sitter Vtol UAV that increases stability against large disturbance. In: *IEEE international conference on robotics and automation (ICRA)*, Anchorage, AK, USA, May 2010, pp. 54–59.
10. Bilodeau P-R and Wong F. Modeling and control of a hovering mini tail-sitter. *Int J Micro Air Veh* 2010; 2: 211–220.
11. Hochstenbach M, Notteboom C, Theys B, et al. Design and control of an unmanned aerial vehicle for autonomous parcel delivery with transition from vertical take-off to forward flight – VertiKUL, a quadcopter tailsitter. *Int J Micro Air Veh* 2015; 7: 395–405.
12. Casau P, Cabecinhas D and Silvestre C. Autonomous transition flight for a vertical take-off and landing aircraft. In: *IEEE conference on decision and control and European control conference (CDC-ECC)*, Orlando, FL, USA, December, 2011, pp. 3974–3979.
13. Park S, Bae J, Kim Y, et al. Fault tolerant flight control system for the tilt-rotor UAV. *J Franklin Instit* 2013; 350: 2535–2559.
14. Lustosa LR, Defay F and Moschetta J-M. Longitudinal study of a tilt-body vehicle: modeling, control and stability analysis. In: *International conference on unmanned aircraft systems (ICUAS)*, Denver, Colorado, USA, 9–12 June 2015, pp. 816–824.
15. Kita K, Konno A and Uchiyama M. Transition between level flight and hovering of a tail-sitter vertical takeoff and landing aerial robot. *Adv Rob* 2012; 24: 763–781.
16. Silva NBF, Fontes JVC, Inoue RS, et al. Dynamic inversion and gain-scheduling control for an autonomous aerial vehicle with multiple flight stages. *J Control Autom Elec Syst* 2018; 29: 328–339.
17. Saeed AS, Younes AB, Cai C, et al. A survey of hybrid unmanned aerial vehicles. *Progr Aerosp Sci* 2018; 98: 91–105.
18. Ritz R and D'Andrea R. A global controller for flying wing tailsitter vehicles. In: *IEEE international conference on robotics and automation (ICRA)*, Singapore, 29 May–3 June 2017 pp. 2731–2738.
19. Knoebel NB and McLain TW. Adaptive quaternion control of a miniature tailsitter UAV. In: *American control conference*, Seattle, WA, USA, June 2008 (ACC), pp.2340–2345.
20. Jung Y and Shim DH. Development and application of controller for transition flight of tail-sitter UAV. *J Intell Rob Syst* 2011; 65: 137–152.
21. Wang W, Zhu J and Kuang M. Design, modelling and hovering control of a tail-sitter with single thrust-vectored propeller. In: *International conference on intelligent robots and systems (IROS)*, Vancouver, BC, Canada, 24–28 September 2017, pp. 5971–5976.
22. Hajiloo A and Rodrigues L. Modeling and backstepping control of under-actuated spherical UAV. In: *IEEE conference on control technology and applications (CCTA),*

Kohala Coast, Hawai'i, USA, 27–30 August 2017, pp. 2069–2074.
23. Fang X, Lin Q, Wang Y, et al. Control strategy design for the transitional mode of tiltrotor UAV. In: *10th IEEE international conference on industrial informatics (INDIN)*, Beijing, China, July 2012, pp. 248–253.
24. Li Z, Zhou W, Liu H, et al. Nonlinear robust flight mode transition control for tail-sitter aircraft. *IEEE Access* 2018; 6: 65909–65921.
25. Smeur EJJ, Bronz M and de Croon GCHE. Incremental control and guidance of hybrid aircraft applied to a tail-sitter unmanned air vehicle. *J Guid Control Dyn* 2019; 43: 1–14.
26. Pucci D, Hamel T, Morin P, et al. Nonlinear feedback control of axisymmetric aerial vehicles. *Automatica* 2015; 53: 72–78.
27. Pucci D, Hamel T, Morin P, et al. Nonlinear control of aerial vehicles subjected to aerodynamic forces. In: *IEEE conference on decision and control (CDC)*, Florence, Italy, 10–13 December 2013, pp.4839–4846.
28. Wang W, Zhu J, Kuang M, et al. Adaptive attitude control for a tail-sitter UAV with single thrust-vectored propeller. In: *IEEE international conference on robotics and automation (ICRA)*, Brisbane, Australia, 21–25 May 2018, pp. 6581–6586.
29. Fliess M and Join C. Model-free control. *Int J Control* 2013; 86: 2228–2252.
30. Join C, Bernier J, Mottelet S, et al. A simple and efficient feedback control strategy for wastewater denitrification. In: *20th world IFAC congress*, Toulouse, France, 9–14 July 2017 (Vol. 50, No. 1) pp. 7657–7662.
31. Rodriguez-Fortun JM, Rotella F, Alfonso J, et al. Model-free control of a 3-DOF piezoelectric nanopositioning platform. In: *52nd IEEE conference on decision and control*, Florence, Italy, 10–13 December 2013, pp. 342–347.
32. Bara O, Fliess M, Join C, et al. Toward a model-free feedback control synthesis for treating acute inflammation. *J Theor Biol* 2018; 448: 26–37.
33. Join C, Robert G and Fliess M. Model-free based water level control for hydroelectric power plants. In: *IFAC conference on control methodologies and technologies for energy efficiency*, Vilamoura, Portugal, 29–31 March 2010 (Vol. 43, No. 1) pp. 134–139.
34. Abouaïssa H, Fliess M and Join C. Fast parametric estimation for macroscopic traffic flow model. In: *17th IFAC world congress*, Seoul, South Korea, 6–11 July 2008, pp. 13040–13045.
35. Chand AN, Kawanishi M and Narikiyo T. Non-linear model-free control of flapping wing flying robot using iPID. In: *IEEE international conference on robotics and automation (ICRA)*, Stockholm, Sweden, 16–20 May 2016, pp. 2930–2937.
36. Al Younes Y, Drak A, Noura H, et al. Robust model-free control applied to a quadrotor UAV. *J Intell Rob Syst* 2016; 84: 37–52.
37. Barth JMO, Condomines J-P, Bronz M, et al. Fixed-wing UAV with transitioning flight capabilities: model-based or model-free control approach? A preliminary study. In: *International conference on unmanned aircraft systems (ICUAS)*, Dallas, TX, USA, USA, 12–15 June 2018, pp. 1157–1164.
38. Barth JMO, Condomines J-P, Moschetta J-M, et al. Model-free control approach for fixed-wing UAVs with uncertain parameters analysis. In: *23rd international conference on methods and models in automation and robotics (MMAR)*, Miedzyzdroje, Poland, 27–30 August 2018, pp. 527–532.
39. Barth JMO, Condomines J-P, Moschetta J-M, et al. Full model-free control architecture for hybrid UAVs. In: *American control conference (ACC)*, Philadelphia, USA, 10–12 July 2019. Unpublished.
40. Drela M. XFOIL: an analysis and design system for low reynolds number airfoils. In: *Conference on low Reynolds number airfoil aerodynamics*, University of Notre Dame, 5–7 June 1989.
41. Lustosa LR, Defaý F and Moschetta J-M. Global singularity-free aerodynamic model for algorithmic flight control of tail sitters. *AIAA J Guid Control Dyn* 2019; 42: 303–316.
42. Lustosa LR. *The Phi-theory approach to flight control design of hybrid vehicles*. Ph.D. dissertation, Institut Supérieur de l'Aéronautique et de l'Espace, École Doctorale Aéronautique-Astronautique, Toulouse, France, ch. 2., 2017.
43. Lafont F, Balmat J-F, Pessel N, et al. A model-free control strategy for an experimental greenhouse with an application to fault accommodation. *Comput Electron Agric* 2015; 110: 139–149.
44. Martin P and Salaun E. Design and implementation of a low-cost observer-based attitude and heading reference system. *Control Eng Pract* 2010; 18: 712–722.
45. Chahl JS, Jain LC, Mizutani A, et al. *Innovations in intelligent machines-1*. Berlin Heidelberg: Springer-Verlag, 2007, pp.181.
46. Smeur EJJ, de Croon GCHE and Chu Q. Cascaded incremental nonlinear dynamic inversion control for MAV disturbance rejection. *Control Eng Pract* 2018; 73: 79–90.
47. Hattenberger G, Bronz M and Gorraz M. Using the paparazzi UAV system for scientific research. In: *International micro air vehicle conference and competition (IMAV)*, Delft, Netherlands, 12–15 August 2014, pp. 247–252.